Chemo-mechanical characterization of a low-pH model cement paste in magnesium bearing environment

Charlotte Dewitte, Laurie Lacarriere, Mejdi Neji, Alexandra Bertron, Alexandre Dauzères

Cement and Concrete Research 184 (2024) 107598

Contents lists available at ScienceDirect

Cement and Concrete Research

journal homepage: www.elsevier.com/locate/cemconres

Chemo-mechanical characterization of a low-pH model cement paste in magnesium bearing environment

Charlotte Dewitte [a,b,*], Laurie Lacarrière [b], Mejdi Neji [a], Alexandra Bertron [b], Alexandre Dauzères [a]

[a] Institut de Radioprotection et de Sûreté Nucléaire (IRSN), PSE-ENV/SPDR/LETIS, F-92260 Fontenay-aux-Roses, France
[b] Université de Toulouse, UPS, INSA, LMDC (Laboratoire Matériaux et Durabilité des Constructions), 135 Avenue de Rangueil, 31077 Toulouse Cedex 04, France

ARTICLE INFO

Keywords:
Blended cement
Degradation
X-ray diffraction
EDX
Microstructure
Mechanical properties

ABSTRACT

In contact with natural waters, concrete can be exposed to the action of magnesium. Mg-attack on the cement paste leads to dissolution of cementitious phases and formation of brucite, hydrotalcite and/or magnesium silicate hydrates (M-S-H). The knowledge of the properties of the latter is limited. In binders with supplementary cementitious materials, M-S-H formation is favoured over that of brucite because of the lower contents of portlandite. To investigate the effects of a magnesium attack on such binders, a low Ca/Si model cement paste was immersed in a 5 mmol/L $MgCl_2$ solution for several months. Energy-dispersive spectrometry analyses coupled with X-ray diffraction and electron probe microanalyses showed Ca leaching, Si preservation and Mg enrichment of the altered zones of the pastes corresponding to the dissolution of C-S-H and formation of M-S-H and amorphous silica. The Mg-enriched zone showed a lower residual Young's modulus than the sound zone as measured by microindentation.

1. Introduction

Worldwide, concrete is used in the construction of civil engineering structures. The desired service life of the structures varies according to the type of use, ranging from fifty years for buildings to hundred or several hundred years for larger infrastructure such as bridges, ports and dams. In the case of deep geological disposal for radioactive waste, the durability of certain concrete components is expected to be several thousand years [1–6].

In an aqueous environment, the chemical attack on concrete can cause changes in the mineralogy of the cement matrix, leading to various detrimental effects like decreased density, formation of cracks, and compromised mechanical properties. It also accelerates the penetration of aggressive species and the release of ions from cementitious systems. This, in turn, lowers the pH and introduces chemical species near the reinforcement, which can be harmful to reinforcement, and lead to its corrosion [7]. In ports and dams, these alterations may result in loss of structural capacity and potential failures which can lead to serious safety threats to the populations nearby, such as collapse of structure and/or resulting in flood [8,9]. In nuclear waste repositories, the durability of concrete is crucial to prevent the release of harmful compounds into the environment. If the concrete deteriorates prematurely, it can jeopardize the repository's integrity, leading to potential leaks and contamination with serious environmental and health consequences [10].

In contact with soft and seawater, concrete is subject to a multi-ionic attack related to the ionic species in these environments (Mg^{2+}, SO_4^{2-}, Cl^-, CO_3^{2-} etc.). Literature reported that contact of concrete with soft or seawater leads to the leaching of the cement matrix in parallel to the penetration of chlorides, sulphates, CO_2 (carbonate), and/or magnesium through concrete [7]. The effect of leaching [13–18], such as the effect of carbonates [19–25] and sulphates [26–29], on the chemo-mechanical behaviour of cementitious material has been studied by many authors. The effect of chlorides [30–38], on the mineralogical, chemical and microstructural changes of the cementitious matrix has also been extensively studied, while the reported research on the effect of the magnesium ions (dissociated from ions that have a strong effect on the matrix, such as sulphates) on those properties is limited. Concerning the attack of magnesium ions, three different Mg-phases can form due to the reaction with the cement matrix: (i) brucite (which tends to form a protective layer) [20,39,40], (ii) hydrotalcite [40] and/or (iii)

* Correspondence to: C. Dewitte, IRSN Institute of Radiation Protection and Nuclear Safety, BP 17, 92262 Fontenay aux Roses, France.
E-mail addresses: cdewitte@insa-toulouse.fr (C. Dewitte), laurie.lacarriere@insa-toulouse.fr (L. Lacarrière), mejdi.neji@irsn.fr (M. Neji), bertron@insa-toulouse.fr (A. Bertron), alexandre.dauzeres@irsn.fr (A. Dauzères).

https://doi.org/10.1016/j.cemconres.2024.107598
Received 21 December 2023; Received in revised form 30 May 2024; Accepted 23 June 2024
Available online 5 July 2024

magnesium silicate hydrates (M-S-H) [20,41–44].

The reaction mechanisms and the type of magnesium phases that precipitate depend notably on the binder nature and the time of exposure to the environment. For intermediate exposure time (several months to years), it was found that for OPC based concrete, the contact with an underground water (carbonates, sulphates and magnesium) leads to the precipitation of a layer of calcite and brucite at the specimen surface [20,45]. In contrast for low CaO/SiO_2 (C/S) cement (such as low pH cements considered for the Cigeo project, the nuclear waste disposal project in France), no protective brucite layer was observed and the attack led to a deep decalcification of the matrix in parallel to the precipitation of M-S-H [20,45]. For longer exposure times (several decades), studies have shown that magnesium attack (by soft or sea water) of cementitious materials with low or no supplementary cementitious materials (C/S > 2) produced an intermediate degradation profile. A brucite layer may have remained but the magnesium enrichment of the matrix was deep and corresponded to the formation of M-S-H [39,44]. Bernard et al. [46,47] studied the solubility of brucite and M-S-H and reported that the brucite is more stable than M-S-H at high pH (from 9.5) and/or high Mg concentration (50 mmol/L) [44,46,47]. In hydrated materials where portlandite is present (like OPC), the pH of the pore solution is around 13.5 [48,49], and under Mg attack, brucite precipitates as it is the most stable phase. When the C/S ratio of the hydrated material is sufficiently low (low-pH concrete for example), no portlandite is present and the pH of the pore solution is lower than for Portland based materials [50,51], which explains the formation of M-S-H observed by Dauzères et al. [20,45]. When the exposure duration is long (several decades, as in marine construction and dams [39,44]), despite the initial formation of a brucite layer, the leaching of the material continues [39], the portlandite is dissolved and the pH drops, which destabilizes the C-S-H, allowing the formation of M-S-H. Several literature reported that in the absence of portlandite in highly substituted binders, the formation of M-S-H is likely to be favoured over that of brucite [20,52].

Literature report that M-S-H is a weakly crystallised phase [53–55], thought to be nanocrystalline, turbostratic phyllosilicate, whose layer charge comes mainly from vacancies in the tetrahedral Si sites [56]. Various studies suggest that M-S-H exhibits a silicate sheet structure that evolves with the M/S ratio [53,57,58]. Increasing the M/S ratio causes depolymerisation of the silicate network, leading to an increase in the gaps within the structure [53]. Studies investigating the microstructural properties of M-S-H [54,59] showed that M-S-H is highly porous with plate-like micro- and mesopores and is sensitive to changes in humidity [59] and the highly porous nature of this phase suggests that M-S-H have poor mechanical properties and would therefore not compensate for the adverse effects of leaching. Some studies have examined the mechanical properties of M-S-H-based pastes [60,61]. In these studies either the M-S-Hs were accompanied by brucite, or additives such as NaHMP, which can modify the structure [62–64]. Therefore the properties observed cannot be directly associated with those of M-S-Hs formed by magnesium attack of cementitious materials.

This study aims to understand the mechanisms of magnesium attack and M-S-H formation in low-calcium cementitious matrices and to study the influence of M-S-H formation on the microstructural and mechanical properties of cementitious matrices. For this purpose, a model cement paste containing mainly C-S-H (no portlandite as in low C/S cementitious pastes) was produced and immersed in a 5 mmol/L $MgCl_2$ solution for 2, 4 and 6 months. The magnesium concentration chosen for this study corresponds to that observed in the pore water of the rock [20]. This paper presents a multi-technique characterization, at the microscopic scale, of the properties of the low-calcium model cement paste exposed to the $MgCl_2$ solution for 2, 4 and 6 months. It combines elemental chemical analysis (energy-dispersive spectrometry analysis – EDS and electron probe microanalysis – EPMA) with analysis of the mineralogical composition (X-ray diffraction – XRD), microstructure (microtomography and N_2 physisorption) and elastic properties (microindentation) of the samples throughout the degradation process in order to jointly explore the chemical, physical and mechanical changes on a micrometre scale during degradation.

2. Materials and methods

2.1. Raw materials and preparation of model cement samples

Model cement pastes (labeled CEMI-sil-col) were produced by the mixing of colloidal silica, Portland cement (CEM I), distilled water (milli-Q water) and superplasticizer (CHRYSO®Fluid Optima 175, provided by Chryso France®). The colloidal silica was Rheomac AS 150 (also called Mastermatrix 150), provided by BASF® in the form of an aqueous suspension (dry extract = 52 ± 2.5 %). The Portland cement was a CEM I 52,5 N CE PM-ES-CP2 NF, from Val d'Azergues d'Azergues (cement's oxide composition provided in Table 1).

The pastes were prepared by mechanical mixing (rotation speed between 140 rd/min and 285 rd/min during 8 min, 450 W). The w/b and the superplasticizer content were optimized so that the mixes can be cast in moulds. Table 2 shows the mix proportions.

At the end of their manufacture, the pastes were kept under endogenous conditions for 11 months (wrapped in parafilm and placed in sealed watertight bags). Then, samples of 4 × 4 × 1 cm^3 were cut, and coated with sealant (Resoltech®, Mastic EPOXY 3030/3036) on the 4 × 1 cm^2 lateral faces to impose unidirectional degradation. The X-ray diffractogram of the sound paste is available in Supplementary data (Fig. 21 in Supplementary data).

2.2. Degradation procedure

Several magnesium solutions have been used in the literature as model media ($MgSO_4$, MgO and $MgCl_2$) for the Mg-attack. A magnesium concentration of 5 mmol/L was chosen as it corresponds to the magnesium concentration of the COx water in deep geological disposal [20] and is an intermediate between the high concentration observed in the marine environment (about 50 mmol/L [44]) and soft water (about 0.5 mmol/L [39]). In addition, the choice of magnesium source was governed by two factors: the pH of the solution and the effect of the counter ions. The high pH of $MgSO_4$ and MgO solutions compared to $MgCl_2$ solution facilitates the formation of an external layer of brucite [46,52], limiting the Mg attack that was intended to be observed. Moreover, the sulphate ions in $MgSO_4$ would cause changes in the cement paste in addition to the magnesium attack [27]. As the main negative effect of $MgCl_2$ counter-ion (Cl) is corrosion of the reinforcement and since the elements of the study are not reinforced, $MgCl_2$ can be used. The pH of the $MgCl_2$ solution is moderately acidic. For an $MgCl_2$ concentration of 5 mmol/L (in equilibrium with atmospheric CO_2), the pH of the solution was around 5.8 (and can slightly evolve during the test, as it can be observed on the pH measured in the attack solution, see Fig. 1). It is only at high $MgCl_2$ concentrations (≥5 wt% or ≥250 mmol/L) that newly formed chloride-based phases are formed in the degraded cement matrix [34–36,77]. Consequently, different sets of samples were immersed in 5 mmol/L $MgCl_2$ solutions in a 60 L closed tank for 2, 4 and 6 months. The solution was constantly agitated and renewed regularly (replenishment times are shown by black vertical dotted lines in Fig. 1). At the end of each exposure time, one or two samples were taken out of the tanks, and several slices (see Fig. 2) cut out to prepare for various characterization tests. The pH of the solutions in the tanks was measured before and after the renewing (see, Fig. 1).

2.3. Multi-technique characterization

A multi-technique characterization procedure was implemented, based on chemical, mineralogical, microstructural and mechanical characterizations of the altered specimens (Fig. 2).

Table 1
Cement oxide composition.

Oxides	SiO_2	Al_2O_3	Fe_2O_3	CaO	MgO	K_2O	Na_2O	SO_3	P_2O_5	CO_2
Mass (%)	20.6	3.60	5.00	64.3	0.70	0.70	0.20	2.70	0.40	0.90

Table 2
Mix proportions of CEMI-sil-col cement paste. Sp/b corresponds to the ratio of superplasticizer to binder mass and w/b to the ratio of water to binder mass.

CEM I (g)	Rhéomac AS 150 (g)	MilliQ-water (g)	Superplasticizer (dry extract) (g)	Sp/b	w/b
590.5	621.7	275.1	10.56	1.20 %	0.65

Sample preparation

Chemical (Energy-dispersive X-ray spectroscopy - EDS and Electron probe microanalysis - EPMA) and mechanical (microindentation) analyses were carried out on flat polished cross sections of the specimens. The polishing (Table 3) for the EPMA was performed without lubricant under compressed air. The polished sections were rinsed with ethanol after each step (see Table 3). For SEM/EDS and microindentation, the polishing protocol is given in Table 4. For sound samples, 7 steps were

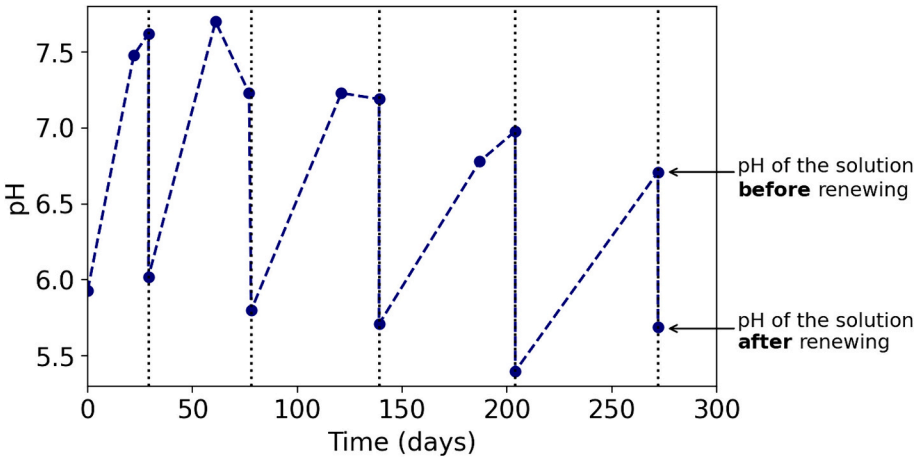

Fig. 1. pH of the 60 L of magnesium solution (5 mmol/L) as a function of time.

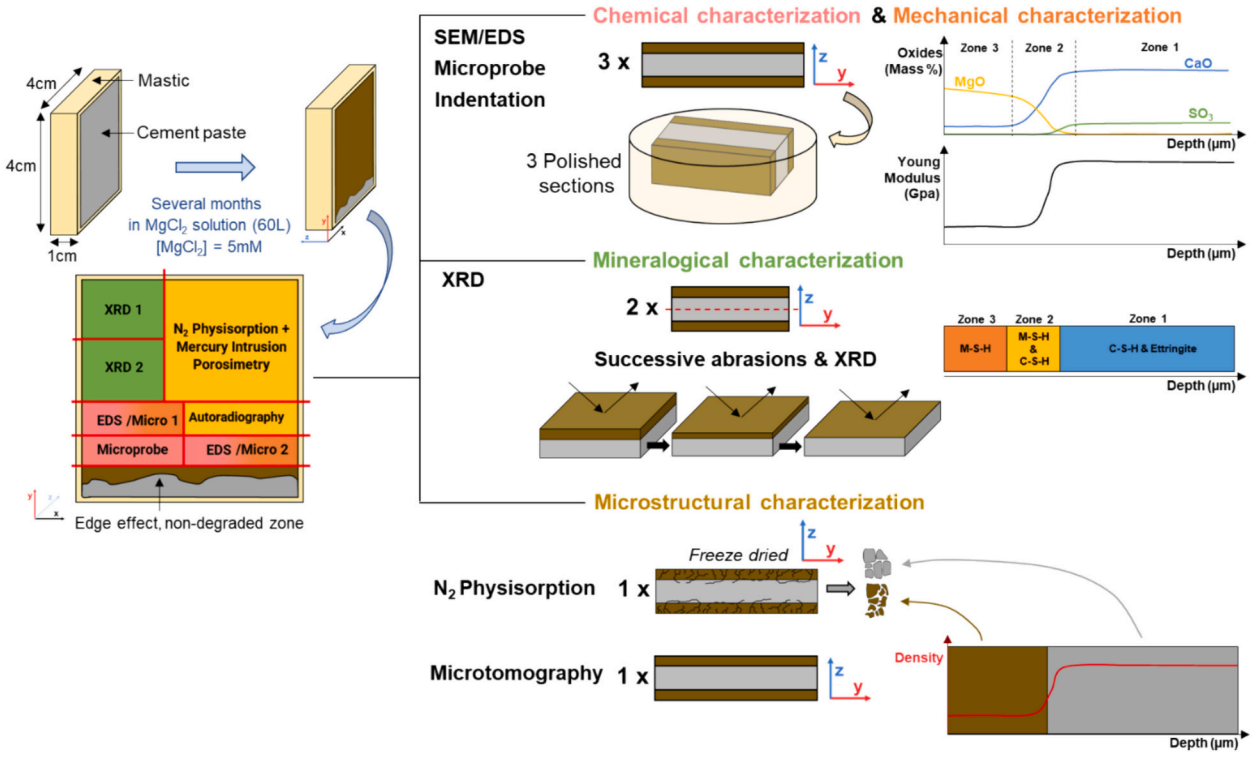

Fig. 2. Schematic representation of the multi-technique characterization protocol. (For interpretation of the references to colour in this figure, the reader is referred to the web version of this article.)

Table 3
Protocol for polishing of cement paste sections for microprobe (EPMA).

Step	Abrasive paper	Speed (rd/min)	Time (min)	Abrasive product
1	800	250	3–4	SiC
2	1200	250	3	SiC
3	4000	250	2	SiC

performed to minimize the roughness. For degraded samples, it was not possible to obtain the same roughness as steps 6 and 7 could not be carried out without altering the surface condition. The microindentation protocol was developed accordingly. All products used for polishing are from Struers©. The polisher used was a Struers LaboPol-2©.

The characterization of the effect of degradation on microstructure (using the N_2 physisorption technique) required a large quantity of samples from the degraded zone. After degradation, as soon as the samples were taken out of the tank, the degraded and the sound zone could be distinguished (Fig. 3a). During the preparation of the samples or during the tests, the degraded zone was cracking due to its high sensitivity to drying. These cracks were located at the limit between the sound zone and the degraded zone (Fig. 3b) and within the degraded zone, perpendicular to the surface exposed to the aggressive solution (Fig. 3c). Therefore, it was possible to separate the sound zone from the degraded one to obtain samples from each zone. Samples were polished at the interface to limit residue from the other zone. An illustration of the location of cracks in relation to the chemical degradation front is proposed in Fig. 4.

For N_2 physisorption, it is necessary to remove the water from the pores to determine the porosity of the samples. Thus, the samples (degraded zone highlighted in Fig. 4) were reduced into pieces of ~0.2 cm^3 and freeze-dried in nitrogen and kept in the freeze dryer (Crios-50, Cryotec) for a least 5 days before being tested.

Chemo-mechanical compatibility

To ensure comparability between the results of chemical and mechanical analyses, the same polished section was used for both tests (EDS and microindentation) and the same areas were studied. To identify the areas observed by EDS, a protocol was developed (see Fig. 5). First, a grid of indents (Fig. 5: 1st step) was identified in the resin, next to the sample. Then, the section was coated with carbon (300 Å) (or gold palladium (277 Å thick)) and observed by SEM. Several zones were chosen, according to their chemical and mechanical interest (Fig. 5: 2nd step). The presence of longitudinal and transverse cracks made it necessary to select areas between two transverse cracks (perpendicular to the surface). Elemental mappings were performed in each of these areas. The longer the exposure time of the specimen to the solution, the deeper the degradation front, requiring the acquisition of several maps next to each other (between 1 and 4 maps). Then, the previously selected areas were identified under the nanoindenter microscope, owing to the traces of the previous indents (Fig. 5: 1st step) in the resin and some remarkable patterns (cracks in the material, bubbles in the resin etc.). Several grids of 4 × 4 indents were made to cover all the zones (Fig. 5: 3rd step). The setting of the indentation parameters was based on the tests on sound material and degraded material to optimize the indentation force and the size of the grid derived. Finally, during the post-treatment, the mechanical results were compared to the chemical results (Fig. 5: 4th step). The metallization layer does not influence the microindentation tests as it is significantly thinner than the impacted zone (h ~ 10 μm). The results from the different analyses were used to establish chemical, microstructural and mechanical property profiles along axes perpendicular to the surface in contact with the $MgCl_2$ solution.

Table 4
Protocol for polishing of cement paste sections for SEM/EDS and microindentation.

Step	Abrasive paper	Retention strength	Speed (rd/min)	Time (min)	Abrasive product	Lubricant + rinsing agent
1	500	30 N	250	2–4	SiC	Ethanol
2	800	30 N	250	30s	SiC	Ethanol
3	1200	30 N	250	1	SiC	Ethanol
4	2000	30 N	250	1 min30	SiC	Ethanol
5	4000	30 N	250	6–8	SiC	DP-Lubricant Brown
6	MD-Dur (3 μm)	30 N	250	8	DP-Suspension-A 3 μm (diamond)	DP-Lubricant Yellow
7	MD-Dur (1 μm)	30 N	250	9	DP-Suspension-A 1 μm (diamond)	DP-Lubricant Yellow

2.3.1. Conditions and settings for mineralogical and chemical analyses

The X-ray diffractometer (XRD) was a Malvern Panalytical Aeris (IRSN, Fontenay-aux-Roses) operating at 600 W, 40 kV and 15 mA, with a Cu anti-cathode (λ ~ 1.54 Å) on powders (sound sample) or solids (degraded sample). For the sound sample and the surface (initial XRD) and sound zone (last XRD) of the degraded sample, the scanning region was in the range 2θ from 5° to 70° with a step size of 0.0109, for a total duration of 1 h (IRSN, Fontenay-aux-Roses). For other abrasive depths of the degraded sample, the total duration of the analysis was reduced to 20 min due to the appearance of cracks in the degraded zone. X-ray diffractograms were plotted against the 2θ angle, noted [2θ] CuKα. The distances to the surface for each abrasion were measured with a digital measuring device with an accuracy of 0.001 mm at one point in the material. However, these measurements only provide an approximate indication of the actual distance, as the material abrasion was conducted manually.

Solid chemical characterizations were carried out with an energy-dispersive spectrometer (EDS) adapted on a scanning electron microscope (SEM, Hitachi S3500N—IRSN, Fontenay-aux-Roses, France) and composed of two EDS Brücker SDD detectors working under a voltage of 15 kV at a working distance of 16.8 mm. The elemental maps were obtained by making hyper-spectral images of a duration of 1 h 47 min on a surface of 1536 × 1152 μm (magnification ×80) with a digital resolution of 3 μm. In addition, electron probe micro-analyses were performed on the sample with an analysis volume of about 5 μm^3 using a Cameca SXFive microprobe (Centre de micro caractérisation Raimond Castaing – UMS 3623, Toulouse, France), operating at 15 kV and 20 nA, equipped with 5 WDS spectrometers. Calibrations were carried out before each series of analyses on synthetic natural controls. The analysed points were chosen one by one to avoid residual anhydrous grains. The microprobe data processing expresses the concentrations of each element in the probed volume as a mass percentage of material (voids excluded). For cementitious materials, these mass percentages are conventionally expressed as the mass percentage of associated oxides. The sum of the oxides is usually around 75 %. The complement to 100 % is largely attributed to bound water in the hydrated phases of the cement matrix (C-S-H, M-S-H etc.). 1 or 2 % can be attributed to carbon in the form of CO_2 or heavy metals [78,79]. Bertron et al. [78] demonstrated that the silicon correction of EPMA data, similar to titanium correction, allows to obtain the absolute variation of the specimen's chemical composition in the altered zone of cementitious materials exposed to acidic and/or leaching environments. The mass percentages of the oxides presented were therefore corrected against the silicon content.

2.3.2. Microstructural analyses

Different types of microstructural analyses (highlighted with yellow in Fig. 2) were conducted to obtain information on the evolution of

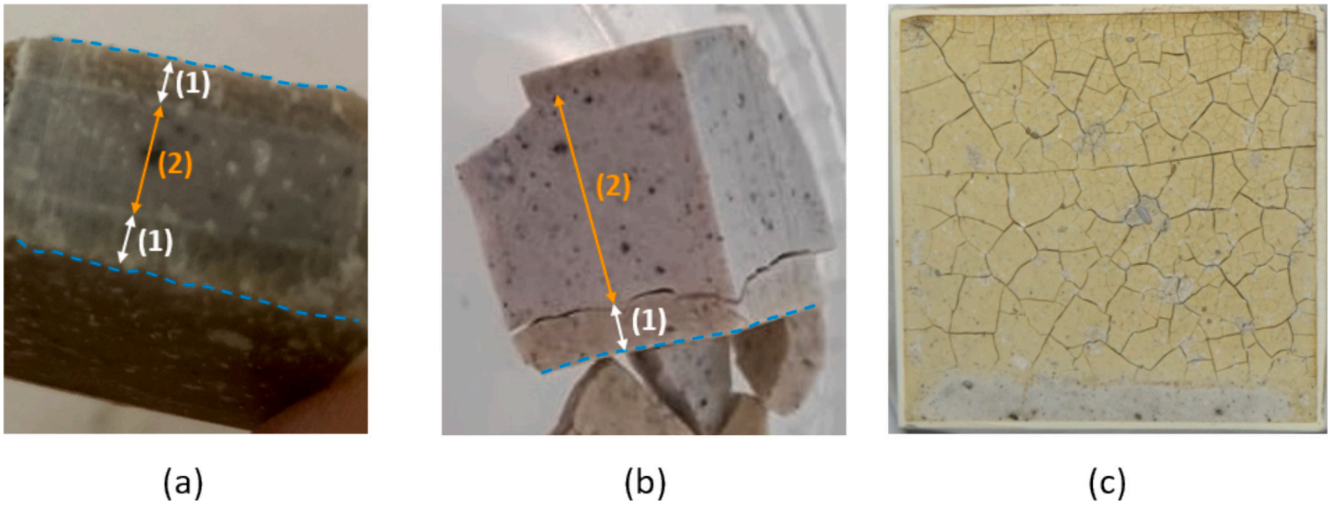

Fig. 3. Visual observation of the Mg enriched zone (1), the sound zone (2) and the exposed surface to aggressive solution (blue dotted line) on a still humid sample (a) and illustration of the shrinkage that occurs at the junction of the two zones on a dry sample (b - profile) and (c - face). (For interpretation of the references to colour in this figure legend, the reader is referred to the web version of this article.)

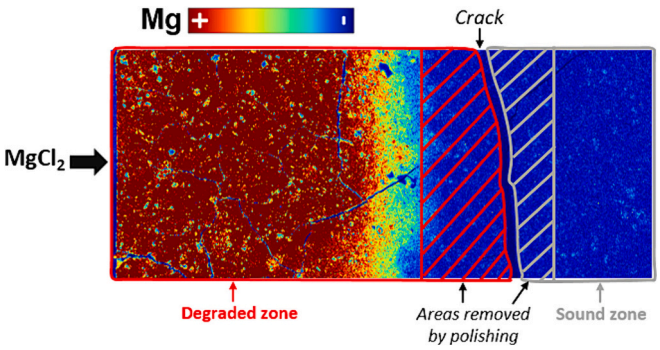

Fig. 4. Illustration on an EDS mapping of the separation of the degraded sample in two parts (sound zone and degraded zone) for MIP and N_2 physisorption.

microstructure from the surface to the core of the degraded sample (X-ray microtomography, autoradiography) and average values (N_2 physisorption, mercury intrusion, water porosity, bulk density measurements) on the selected zones.

2.3.2.1. X-ray microtomography. Small pieces (~100 mm^3) of the degraded samples were cut and placed under parafilm directly at the exit of the degradation tanks. Then, the samples were analysed by X-ray microtomography using a SkyScan 1272 (Bruker microCT N.V, Fontenay-aux-Roses). The samples remained under parafilm throughout the test. The parameters of the X-ray tube (100 kV, 100 mA) were set to optimize the contrast between the different phases and the pores. An angular step of 0.1° was used to acquire radiographs (total acquisition time: about 20 h). A spatial resolution of 2 μm was obtained.

2.3.2.2. Nitrogen physisorption. Nitrogen sorption isotherms were measured using a 3Flex Micromeritics (MIC271002 REV B) instrument equipped with version 4.05 of the 3Flex software (IRSN, Fontenay aux Roses). Before the analysis, freeze-dried samples were heated at 45 °C under a vacuum in a sample cell for 4 h to remove water and other physically adsorbed volatile material from the sample's surface. The samples underwent nitrogen adsorption followed by desorption for a total of approximately 20 h. The specific surface area ($SSA_{B.E.T}$) of the samples was calculated by applying the Brunauer-Emmett-Teller (B.E.T.) equation in the p/p^0 range of 0.05 to 0.2. The pore distribution was obtained by the Barrett-Joyner-Halenda (BJH) method [80].

2.3.3. Elastic properties characterizations

To determine the elastic properties of the degraded sample at the mesoscopic scale, microindentation measurements were performed locally on the sample kept in $MgCl_2$ for 6 months.

Indentation refers to the contact between a hard material with known mechanical properties (the indenter), and the material under investigation whose properties are unknown. The depth of penetration is measured continuously during the loading process. A stress/depth curve is obtained (Fig. 6). P_{max} and h_{max} are the maximal load and depth respectively.

The reduced modulus of elasticity (E_r) of the material can be determined from the slope of the unloading of the indentation curve using Eq. (1):

$$E_r = \frac{\sqrt{\pi}*S}{2*\sqrt{A_c}} \quad (1)$$

where

- S is the contact stiffness of the upper part measured experimentally during the unloading phase of the test
- A_c is the projected contact area from the tip on the indented material

A_c is estimated from the contact depth (h_c). Fig. 7 illustrates the experiment and the notations. In the case of a Berkovich tip, $A_c/h_c^2 = 24{,}50$ [82,83] and h_c is expressed by Eq. (2):

$$h_c = h_{max} - \frac{2}{\pi}.\frac{(\pi-2)*P_{max}}{S} \quad (2)$$

For materials with unknown or variable Poisson's ratios (as degraded materials with properties gradients), it is more convenient to calculate the plane strain indentation modulus E_{PSIM} ($E_{IT}/(1-\nu^2)$) instead of the indentation modulus. E_{PSIM} can be determined by Eq. (3):

$$E_{PSIM} = \frac{E_{IT}}{(1-\nu^2)} = \frac{E_r*E_i}{E_i - E_r*(1-\nu_i^2)} \quad (3)$$

where:

- E_{PSIM} is the plane strain indentation modulus
- E_i is the modulus of elasticity of the indenter
- E_{IT} is the modulus of elasticity of the material under investigation

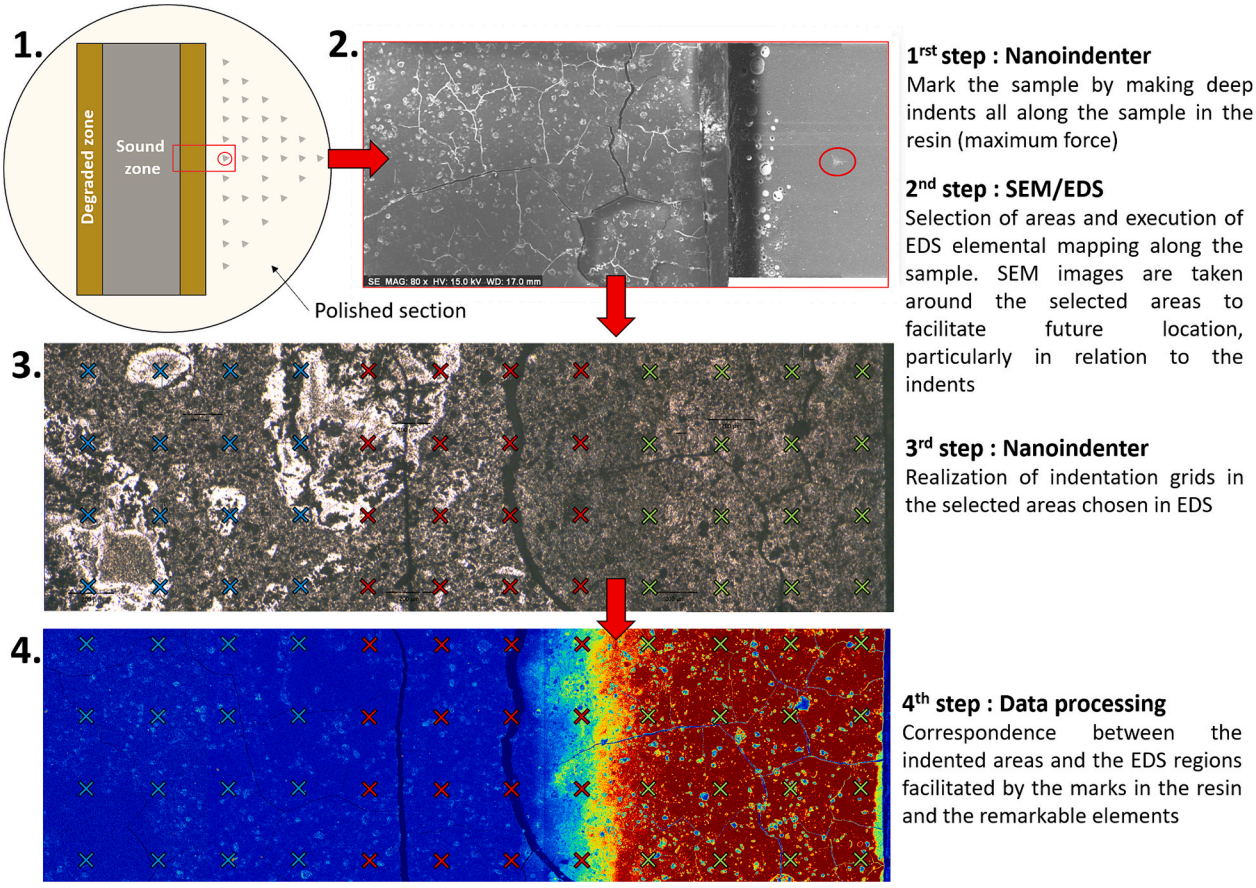

Fig. 5. Protocol for coupled chemo-mechanical analysis.

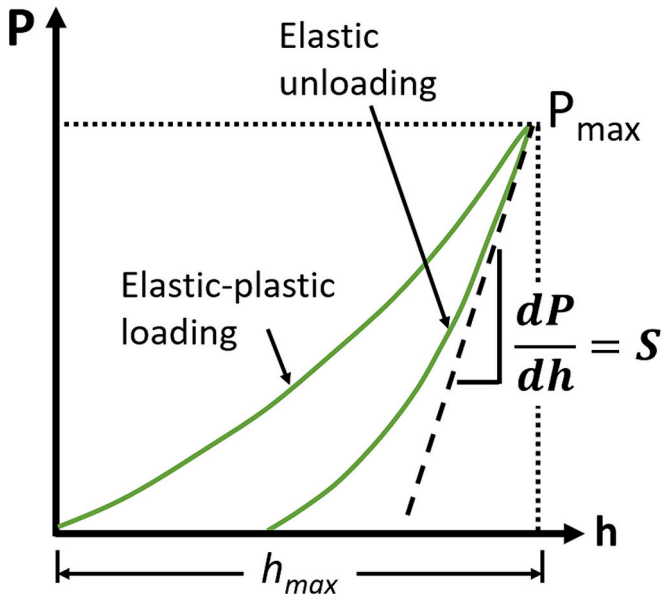

Fig. 6. Typical load-depth curves in indentation experiment. Adapted from [81].

- ν is the Poisson's ratio of the tested material
- ν_i is the Poisson's ratio of the indenter.

The indentation modulus reflects the properties of the material within the interaction volume directly underneath and around the indent (illustrated in the yellow hatch in Fig. 7). The interaction volume depends on the applied load and the indented depth (h_{max}). It extends, in the shallow subsurface, to 3–4 times the indented depth (h_{max}) [75,84,85]. When indentation is performed on hardened cement pastes, the material response depends on the properties and volume fractions of the different hydrated and non-hydrated elements present in the interaction volume (C-S-H, portlandite, ettringite, clinker, porosity etc.). The higher the applied load, the higher the indented depth and the larger the interaction volume. A broader range of pore sizes is then included in the measurement volume and, for a homogeneous material, the indentation modulus decreases [86]. Fig. 7(a) and (c) correspond to a smaller interaction volume (yellow semi-circle on Fig. 7(c)) than the characteristic length (D) of the biggest inhomogeneity at the level considered. Fig. 7(b) and (d) correspond to a bigger interaction volume than the characteristic length of the biggest inhomogeneity at the level considered.

Indentation tests were carried out with a nano-indenter (NHT^3, Anton Paar®—IRSN, Fontenay-aux-Roses, France) with a Berkovich tip on the polished section of the cementitious samples (same polishing protocol as for SEM/EDS, see Table 4). Due to the cracking phenomenon appearing on the sample after it was placed in $MgCl_2$ for 6 months, and the high porosity in the degraded zone, the polished section was not flat enough to perform indentation tests with low forces (allowing a small penetration depth). Consequently, the indentation force was increased until the tests were no longer impacted by the roughness of the sample. The microindentation tests were force controlled (Max load = 200 mN, loading rate = 100 mN/min, Pause = 10 s). To avoid the influence of one indentation on the other, the tests should be separated by a minimum distance (Δ), which is discussed next. The recommended distance to avoid overlapping of the elastic domains of each indentation is at least 30 times the maximum depth [83]. In these tests, the penetration depth

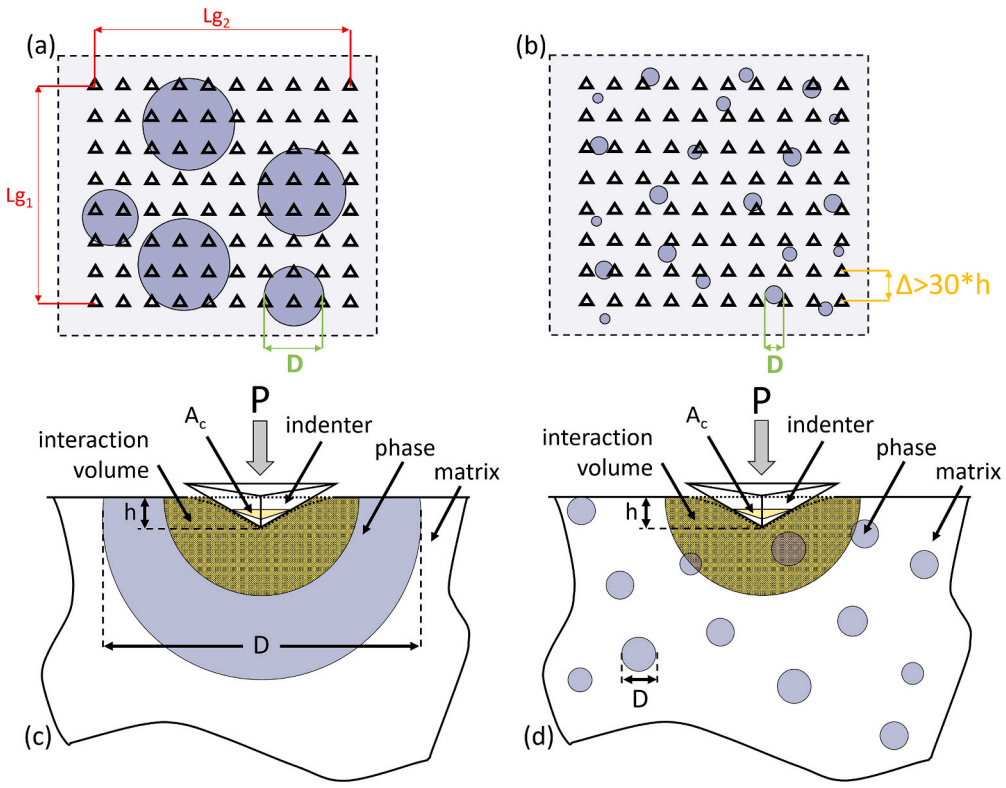

Fig. 7. Grid indentation and indenter scheme on a heterogeneous system where the probed microvolume (cross-hatched regions below the indenter) is either (a–c) smaller or (b–d) larger than the characteristic length scale, D, of the phase of interest. The triangles correspond to the indents. Other symbols are defined in the text. Adapted from [83,84,87].

was about 10 μm, so the indents were spaced 300 μm apart, resulting in indentation grids of 4 × 14 indents. As the polished sections used for microindentation are the same for SEM/EDS analyses, a thin layer of carbon is present on the surface of the sample. Because the indented depth is between 5 and 10 μm, the thickness of carbon (approximately 300 Å) is considered as non-impacting the measurements.

3. Results

3.1. Mineralogical and chemical characterization

3.1.1. EDS

To visualize the degradation front and characterize the chemical evolution in the degraded samples, SEM/EDS analyses were performed

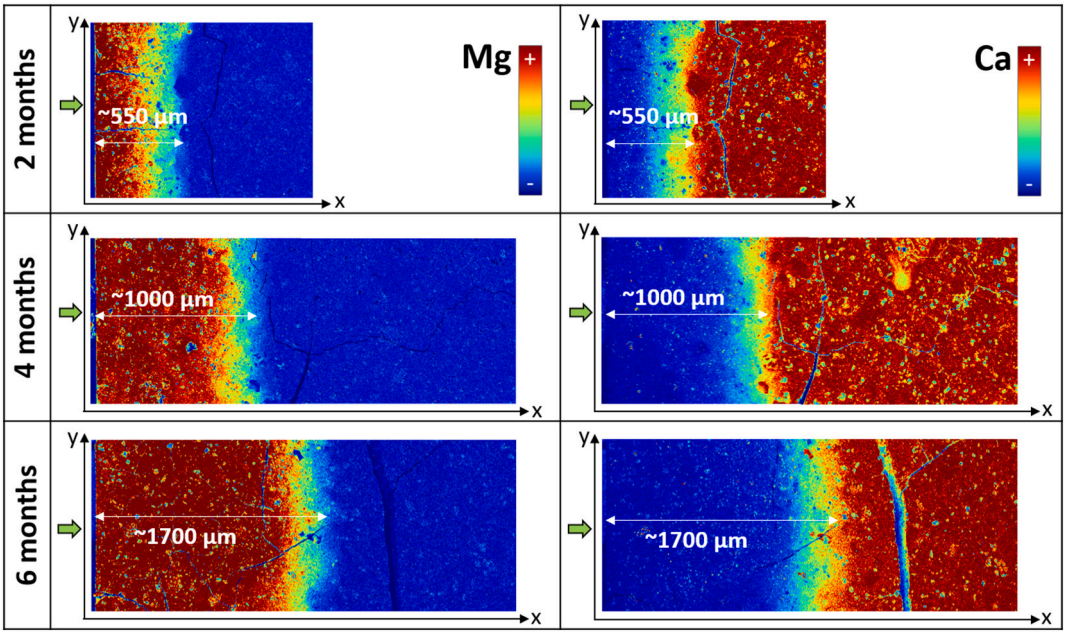

Fig. 8. Elemental maps (EDS) in calcium and magnesium of a low-pH model cement paste immersed in a solution with [$MgCl_2$] = 5 mmol/L for 2, 4 or 6 months.

at different exposure times (2, 4 and 6 months). Fig. 8 shows the EDS magnesium and calcium maps. The exposed surfaces to the $MgCl_2$ solution are on the left (see the green arrow in Fig. 8). For each sample, the extreme values of the scale are calibrated in the sound and degraded zones. The colour shades are not directly comparable from one Fig. to another. The abscissa and ordinate are marked x and y on each of the figures. As discussed in Section 2.3, cracks appear on the samples and are visible on EDS maps. The estimated depth of the degradation front observed in the EDS maps (Fig. 8) was plotted on each map using a white arrow.

Fig. 9 shows the profiles of Ca/Si and Mg/Si intensity ratios calculated from the EDS elemental mappings. The curves are obtained by averaging the ratios of intensities of the elements (Ca/Si and Mg/Si) by columns of pixels: each value at x is the average over all points at that x with y varying between 0 and 768 µm. To limit the impact of the holes and the crack (around 1130 and 2000 um), values of Mg/Si and Ca/Si out of the interval [0;3] at each x were excluded. A figure with the raw data is available in the Supplementary data (Fig. 24).

EDS maps and profiles show a Mg enrichment of the cement paste in conjunction with Ca leaching (Figs. 8 and 9). As the degradation time increases, the depth of the magnesium-enriched zone (Z3) increased from a few tens of micrometres (2 months) to 1100 µm (6 months) (Fig. 9c). The slope of the curve was approximately negligible (zero) in the central part of Zone 3. At the surface, the Mg/Si remained constant (and high) with time. The Mg enrichment was more pronounced near the surface, in the first 100 µm, reaching Mg/Si of about 0.8 for the 3 exposure times.

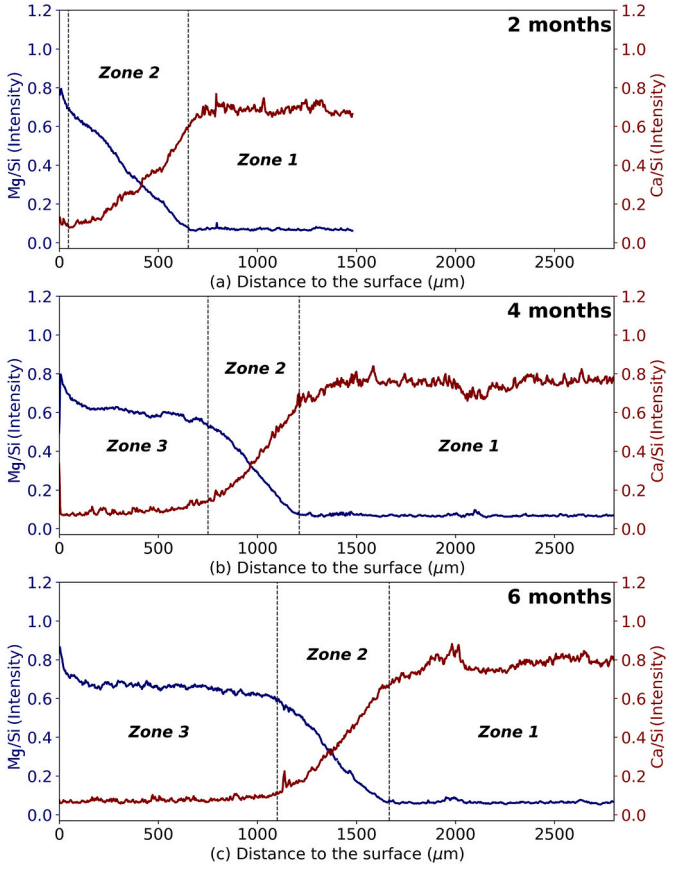

Fig. 9. Mg/Si and Ca/Si intensity ratios calculated from solid chemical composition (EDS) of a low-pH model cement paste immersed in a solution with 5 mmol/L [$MgCl_2$] for (a) 2 months, (b) 4 months and (c) 6 months along the depth from the surface of the specimen. Each value at x is the average over all points at that x with y varying between 0 and L (i.e., the width of the map in Fig. 8).

As EDS was not quantitative, EPMA has been completed.

3.1.2. EPMA

Fig. 10 shows the major oxide composition profiles of the sample degraded for 6 months obtained using EPMA, after correction of the contents with respect to silica. Unprocessed data are available in Supplementary data (Fig. 22). The quantity of silica in the sound zone is averaged (here over 240 points) and then a correction factor is calculated at each point by dividing the quantity of silica at that point by the averaged value. Finally, at each point, the quantity of each oxide is divided by the correction factor. From the core of the specimen to the exposed surface, the following three zones could be identified, which is supporting the observations from EDS:

- the sound zone (Z1) from the core to 1750 µm from the surface
- a transition zone (Z2) between 1100 and 1750 µm. The Ca content decreases while the Mg content increases.
- a zone strongly decalcified and enriched in Mg (Z3). The Ca content remained constant and equal to 5 wt% while the Mg content continued to increase. As in the case of other types of attacks leading to leaching [78], the leaching front of sulphate species is an indicator of the beginning of the highly degraded zone. A drop in the sulphur content is observed around 1750 µm from the surface which corresponded to the limit of the decalcification zone.

The amount of Mg in the sound zone was negligible, which was consistent with the MgO content of the cement (0.70 wt%). The Al content remained constant along the degradation depth (Fig. 10). No enrichment in chloride and no variation in Fe content were observed (Fig. 23 in Supplementary data). Therefore, chloride ions did not seem to bind to the matrix.

Profiles of M/S (MgO/SiO_2) and C/S (CaO/SiO_2) molar ratios (Fig. 11) according to the distance from the exposed surface were obtained from the EPMA profiles for the sample degraded for 6 months in the 5 mM $MgCl_2$ solution.

On Fig. 11, Zone 1, the sound zone, showed a plateau of C/S at 0.9 and M/S at 0.05. The atomic C/S ratio obtained from EPMA analyses is consistent with the theoretical one of the model pastes, the Ca/Si atomic ratio of the mix being 0.94. Zone 2, corresponding to the transition zone, showed a sigmoid decrease of C/S in conjunction with a sigmoid growth of M/S. In the degraded zone (Z3), the atomic M/S ratio increases slowly until it reaches a ratio of 0.8 at the surface. The slope of the M/S curve increases as the measurement is close to the surface, indicating a larger Mg enrichment of the paste in direct contact with the solution, as detected in EDS (Fig. 9). It should be noted that the C/S and M/S ratios correspond to the ratio between all the calcium or magnesium and all the silicon present in the solid phase, which can correspond to a mixture of several species (amorphous silica, M-S-H etc.).

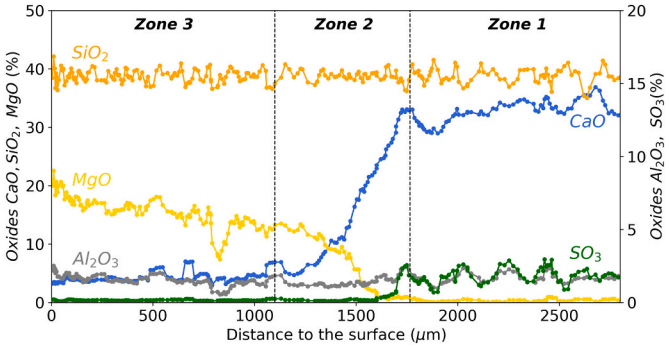

Fig. 10. Chemical composition of oxides of a low-pH model cement paste, immersed in a solution with [$MgCl_2$] = 5 mmol/L for 6 months according to the distance to the surface of the specimen (analysis by EPMA, corrected).

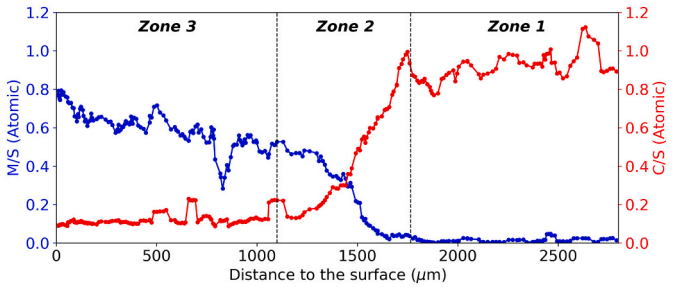

Fig. 11. M/S and C/S atomic ratios calculated from EPMA data on a low-pH model cement paste immersed in a solution with [$MgCl_2$] = 5 mmol/L for 6 months.

3.1.3. XRD

Mineralogical characterization by XRD is presented in Fig. 12. The figure is divided into three sets of diffractograms labeled as (a), (b), and (c), corresponding to the results obtained after 2, 4, and 6 months of paste degradation, respectively. In each set, the diffractograms are arranged in order of abrasion. The surface of the sample prior to abrasion is positioned at the top, followed by the diffractograms obtained through successive abrasions until reaching the sound zone. The indexing of the X-ray peaks for the C-S-H (green circles) and M-S-H (red triangles) phases is based on [47]. Whatever the time frame and depth of degradation, the majority of phases detected by XRD are poorly crystallised phases (C-S-H and/or M-S-H). In the sound zone, the only crystalline phase detected was ettringite. Also, in the degraded zone, crystalline aluminous phases were nil or negligible.

Three zones can be defined according to their mineralogical composition, the location of the boundaries between these zones changing as the reaction front progresses within the paste. (i) In the sound zone, the paste was mostly composed of C-S-H and some ettringite. Additionally, no peaks associated with portlandite were visible in the sound paste (Fig. 21 in Supplementary data). (ii) In the intermediate zone, M-S-H and C-S-H coexisted. (iii) In the outer zone, X-Ray diffractograms displayed only the humps associated with M-S-H and no

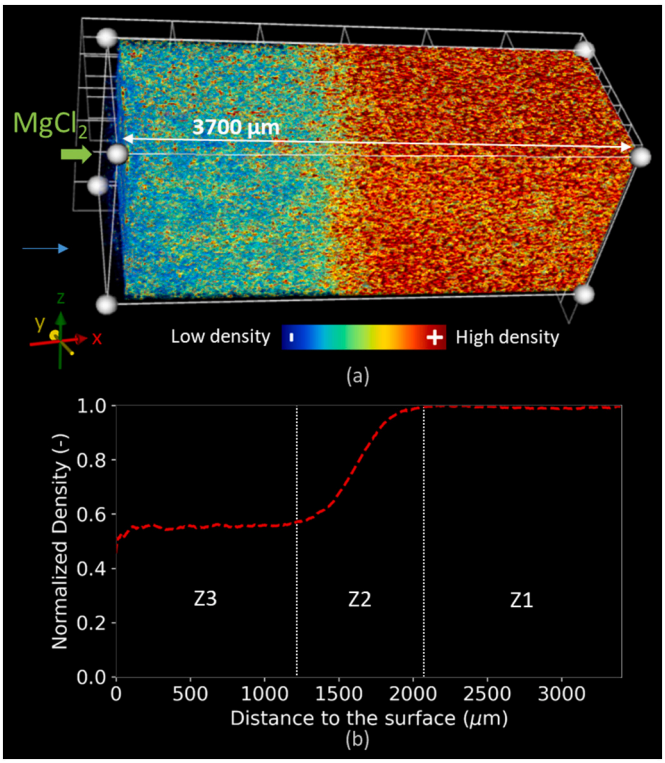

Fig. 13. (a) 3D visualization of the density and (b) density profile averaged in the (y,z) plane for each x, after micro-tomography measurements for a low-pH model cement paste, immersed in a solution with [$MgCl_2$] = 5 mmol/L for 6 months.

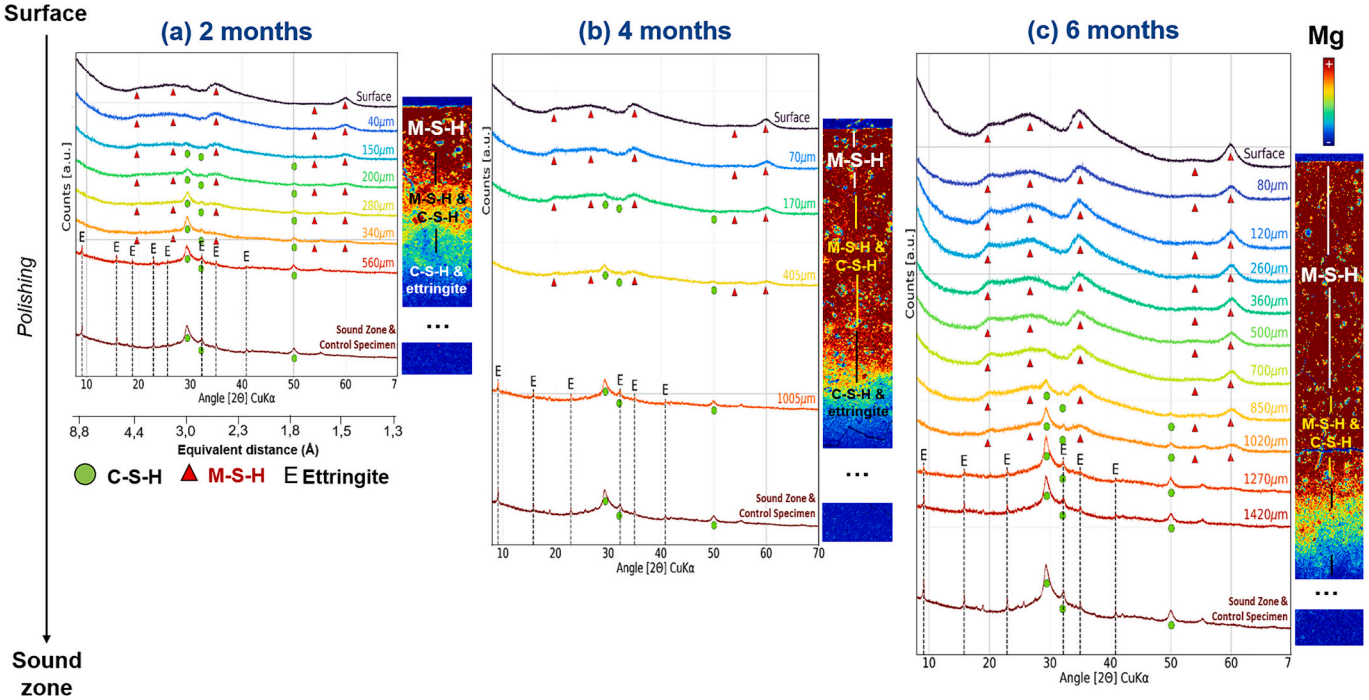

Fig. 12. X-ray diffractograms according to the distance to the surface of a low-pH model cement paste placed in a solution with [MgCl2] = 5 mmol/L for (a) 2 months, (b) 4 months and (c) 6 months associated with EDS maps. The control specimen's XRD was acquired on powder, while the others were on solids.

brucite was detected.

3.2. Microstructure

Fig. 13 illustrates the results of microtomography performed on the 6-month degraded sample. Fig. 13(a) represents the 3D distribution of the density and Fig. 13(b) shows the associated 1D density profile of the 6-month degraded sample. To realize the 1D density profile, the intensity is averaged on each plane (y,z) for each x of Fig. 13(a). To obtain a normalized density, the highest point of the curve is considered the base value and the average of each plane (y,z) is divided by this value. The density presented here is the signal intensity at each point (value related to the absorption coefficient of the material) normalized to the maximum value of the sample.

As with previous characterization methods, three zones are observed to emerge in the micro-tomography results. The sound zone (Z1) showed the highest density, then the density decreased significantly in the transition zone (Z2). The external zone (Z3), which was in contact with the aggressive solution, exhibited a density half of that in the sound zone.

3.3. Elastic properties

To calculate Young's modulus from the indentation experiment, it is needed to know the Poisson's coefficient (see Eq. (3)). As in the degraded zone the evolution of the Poisson's coefficient was not predictable, the results were expressed as plane strain indentation modulus E_{PSIM} (equal to $E_{IT}/(1-\nu^2)$) (GPa). Fig. 14(a) shows the indentation grids performed on the degraded sample for 6 months on the associated Mg EDS maps. The 2D distribution of the plane strain indentation modulus is displayed in Fig. 14(b). To obtain a 1D profile, the values have been averaged for each x (by column) and Fig. 14(c) exhibits the results.

When indentation was performed in the room's environment, the samples were exposed to the air – leading to the cracking of the deteriorated zones and making the characterization difficult (see Section 2.2). The cracking of the sample implied a non-flat area and an extended disturbed area. As a consequence, some indents performed in Cells 3, 5, 9, 10, 16, 17, 22, 23, 30, and 29 (Fig. 14a and b) did not yield results. The number of points where the results were valid in the left cracking zone (Zones 5, 8, 11, 18 and 29 on Fig. 14 - $1600 < x < 2200$ µm) were indeed significantly lower than those in the other locations and could not be considered as representative (only 4 out of 20 indents were successful). Moreover, the 2D representation of the results depicted in Fig. 14(b) shows that there are outliers. Fig. 14(c) shows the results after removing the outliers by using the interquartile range method (as for the sound paste). Fig. 14(c) shows the dispersion of the data with the mean, the median and the standard deviation (greyed beam). The vertical bars of the graph show the number of points used for calculating the mean and median for each of the x-positions.

From the sorted data, it is observed that the elastic property profile (Fig. 14c) matches the chemical and porosity trends (presented earlier in Figs. 9, 13). After removing outliers, Zone 3 of the 6-month sample exhibited even elastic modulus values (E_{PSIM}) and was relatively large (1100 µm wide). The elastic characteristics of Zone 3 were around 2.0 GPa with a standard deviation of 1.0. The sound zone (Z1) had elastic properties (E_{PSIM}) around 11.4 GPa with a standard deviation of 2.2 GPa. Therefore, mechanical properties of the cement paste under Mg attack were significantly reduced (E_{PSIM} (Zone 3)/E_{PSIM} (Zone 1) = 17.5 %).

4. Discussion

Fig. 15 summarizes the main chemical, microstructural and mechanical results of the sample immersed for 6 months in the 5 mmol/L $MgCl_2$ solution. Fig. 15 highlights the correspondence between loss of mechanical properties, reduction in density, decalcification and Mg enrichment in the altered zone of the specimen. The boundary between

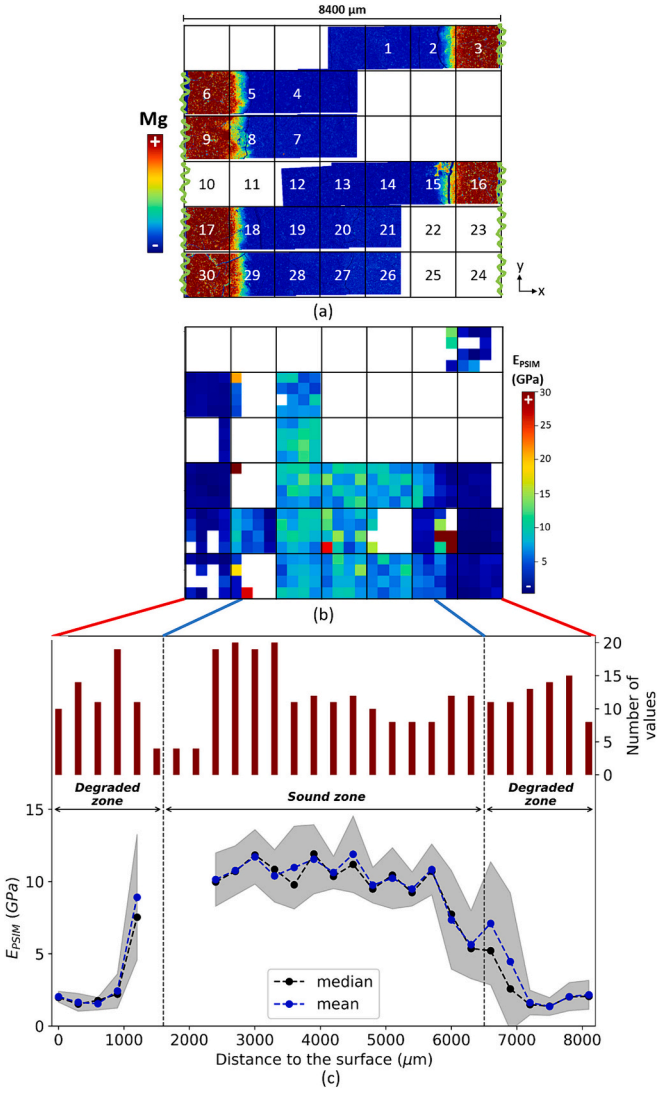

Fig. 14. (a) Localisation of 4 × 4 micro indents grids on Mg EDS Maps, (b) plane strain indentation modulus E_{PSIM} results associated and (c) micro-indentation data averaged per column, without outliers.

Zone 1 (sound zone) and Zone 2 (transition zone) observed in EPMA (Fig. 15(b)) corresponds to the starting of the degraded zone in the other techniques (EDS, microtomography and microindentation). The next paragraphs discuss the chemical and physical origin of this loss of properties, while a new phase, M-S-H, is formed when C-S-H are leached (see Fig. 12).

4.1. Evolution of the chemical and mineralogical composition

4.1.1. Mineralogical composition

Results from EDS (Fig. 9), EPMA (Fig. 10) and XRD (Fig. 12) showed that three zones could be distinguished in the exposed samples: a sound zone, a transition zone and a degraded zone. The boundaries between zones shift with the duration of exposure but remain comparable between XRD and EDS (see Figs. 9 and 12).

4.1.1.1. Sound zone. Only C-S-H and ettringite are visible on the XRD. EPMA (Z1 Fig. 10) and EDS (Z1 Fig. 9) experiments confirm this observation by revealing that Ca and Si predominate, with a trace of Al and S.

4.1.1.2. Degraded zone. XRD (Fig. 12) revealed only M-S-H, and EDS

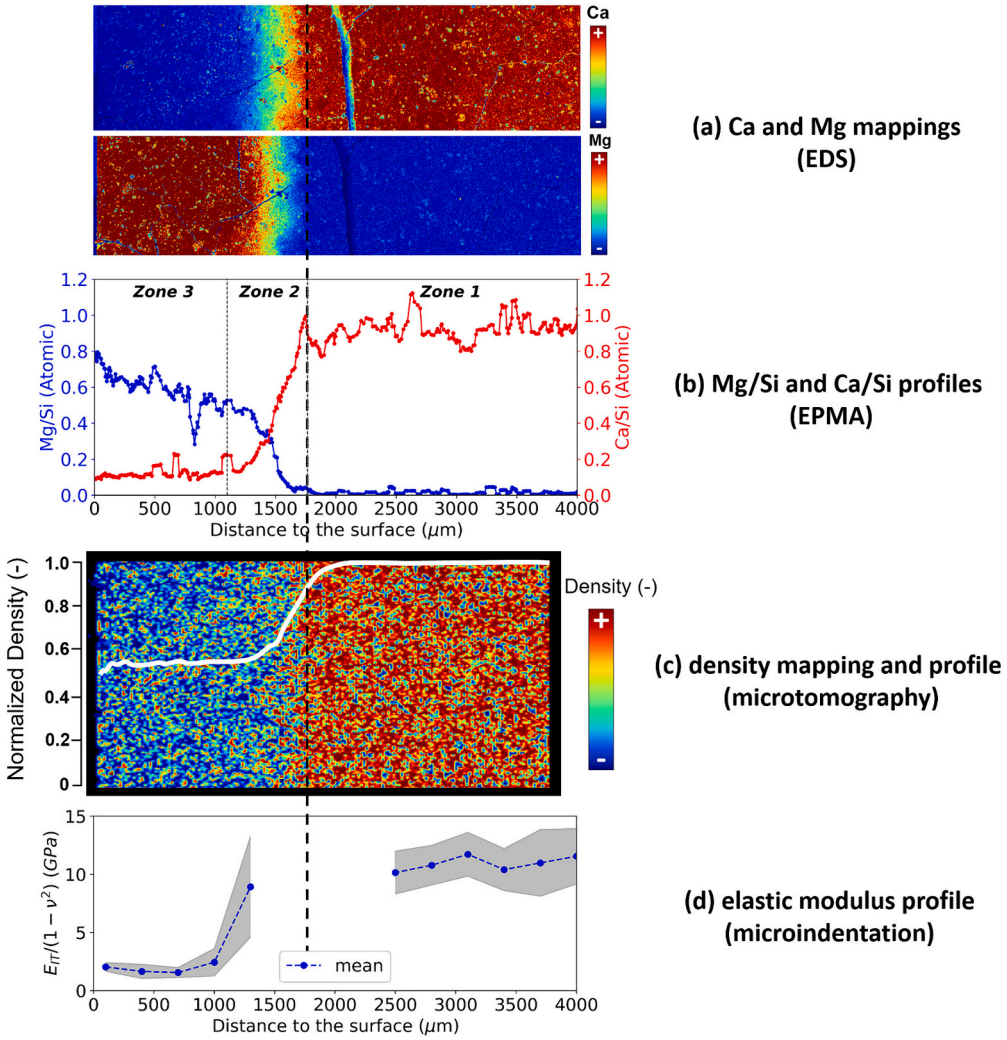

Fig. 15. Multi-technique characterization of a low-pH model cement paste immersed for 6 months in a solution with [$MgCl_2$] = 5 mmol/L, (a) Ca and Mg mappings (EDS), (b) Mg/Si and Ca/Si profiles (EPMA), (c) density mapping and profile (microtomography) and (d) elastic modulus profile (microindentation).

(Z3 Fig. 9) and EPMA (Z3 Fig. 10) confirmed Mg and Si are the major elements of this zone. EPMA revealed that the Al was preserved in this zone, but it was not incorporated in a crystallised phase (Fig. 12) and will be explored later in this paper. When the degraded zone is sufficiently extended (4 and 6 months), the EDS indicates a similar intensity ratio – indicating that the average composition of the degraded zone does not change with exposure time (Fig. 9(b) and (c)).

4.1.1.3. Transition zone. The coexistence of C-S-H and M-S-H was confirmed in the transition zone by XRD (Fig. 12), EPMA (Z2 Fig. 10), and EDS (Z2 Fig. 9). Fig. 9 shows that the degraded depth after 6 months was 1.7 mm. This degraded depth is consistent with that observed in [20], where the degraded depth reached 1.6 mm after 5 months of exposure of an industrial low-pH material (with a porosity of 35 % against 51 % for the model paste) to a solution reproducing the pore solution of a Callovo-Oxfordian (COX) rock ([Mg] = 6.7 mM). However, this remains a significant degraded depth for an attack that is initially assumed to be slightly aggressive (XA1 within the meaning of FD P 18-011 [88] and NF EN 206 [89]).

The progressive enrichment of the paste observed by EDS (Fig. 8) is consistent with the M-S-H formation pattern observed in studies of magnesium attacks on cementitious materials [41,44,45]. The behaviour observed is specific to low-pH (or low C/S) pastes. Magnesium attack on this type of material does not cause brucite formation, even with short-term exposure (2 months). This is confirmed by the absence of brucite in the degraded material (not detected in XRD, see Fig. 12), the low M/S ratio calculated from EPMA data (Fig. 11) and the absence of a Mg-rich layer on the surface of the samples on EDS maps (Fig. 8). In the absence of portlandite in the sound paste (low pH), brucite does not form and does not play its 'protective' role. Magnesium then penetrates deep into the paste (up to 1700 μm in 6 months) and M-S-H is formed. This study showed that the magnesium-enriched zone has a stable composition despite the increase in exposure time to the magnesium medium. Only the width of the magnesium-enriched zone increased with exposure time.

4.1.2. Stoichiometry of phases produced by degradation and incorporation of Ca in solid phases

As EPMA is quantitative, it can be combined with XRD observations to analyse the stoichiometry of the phases formed during degradation. As the EPMA was carried out only on the 6-month sample, the discussion focuses on this sample. The XRD results (Fig. 12) show the presence of M-S-H in Zone 3. At the surface of the degraded sample, the EPMA (Fig. 11) shows a M/S of 0.78 consistent with the possible stoichiometries of M-S-H according to Bernard [47,90]. Similar M/S were observed by Liu et al. [52] when they exposed suspensions of C-S-H to 50 mM $MgCl_2$ solutions.

A stoichiometric calculation of M-S-H quantity from the Mg ($n_{Mg_{solid}}$)

EPMA contents is thus achievable following the Eq. (4).

$$n_{Mg_{solid}} = 0.78 * n_{MSH} \quad (4)$$

with n_{MSH} the calculated quantity of M-S-H.

As in most of Zone 3 and Zone 2 (Fig. 11) the M/S was <0.78, which is the lowest M/S to guarantee M-S-H stability [53]. The presence of an amorphous siliceous solid phase not detected or not distinguished from M-S-H humps by x-ray seems likely, as in pure leaching [18]. On X-ray diffractograms, amorphous silica manifests itself through the hump ranging from 20 to 30 [2θ] CuKα, which may superimpose with the humps associated with M-S-H in this range. Using the assumption of amorphous silica in the degraded zone, the amount of amorphous silica ($n_{am.SiO_2}$) can be calculated using Eq. (5).

$$n_{Si\,solid} = n_{MSH} + n_{am.SiO_2} \quad (5)$$

with $n_{Si\,solid}$ the Si EPMA content.

Fig. 16 shows the results of the stoichiometric calculations performed. The silica content increased when approaching the transition zone (Z2). This increase is consistent with the phenomenon of dissolution-precipitation where the dissolution of C-S-H is expected, creating a Si gel and the precipitation of M-S-H from the Mg diffusion and chemical reaction [41,44,45].

EPMA (Fig. 10) reveals a calcium content of 4 % in solid phases in the degraded area (Z3) which raised questions about the incorporation of calcium in the solid phases (in Z3). The C/S_{total} molar ratio measured in EPMA reached 0.1 (Fig. 11). As no C-S-H was detected by XRD in this zone, the calcium could be in the M-S-H and/or in the amorphous siliceous phase (Fig. 12). In the literature [47,57,90], it was observed that calcium can be incorporated in M-S-H in small quantities (M/S = 0.78 and C/S = 0.05 up to 0.1). Liu et al. observed that the incorporation of a small amount of Ca (C/S < 0.2) into M-S-H did not alter the structure of M-S-H [52]. In the case of pure leaching, remaining calcium was also observed in the degraded zone (probably incorporated in amorphous silica gel) with a C/S ≈ 0.1 [18].

Considering that calcium can be incorporated into silica ($C/S_{am.\ SiO2}$) and M-S-H (C/S_{MSH}), the amount of calcium incorporated ($n_{Ca\,solid}$) can be calculated using Eq. (6):

$$n_{Ca\,solid} = \frac{C}{S_{MSH}} \times n_{MSH} + \frac{C}{S_{am.SiO_2}} \times n_{am.SiO_2} \quad (6)$$

with $\frac{C}{S_{MSH}}$ and $\frac{C}{S_{am.SiO_2}}$ the molar ratio of CaO on SiO_2 in M-S-H and amorphous silica respectively.

Calculations were carried out to find the optimum [$C/S_{am.\ SiO2}$, C/S_{MSH}] pair to recover the amount of calcium measured by EPMA, in accordance with the literature data discussed in the previous paragraph. Fig. 17 illustrates the calcium contents in the solid phases calculated for the 9 best pairs of [$C/S_{am.\ SiO2}$, C/S_{MSH}] compared to the EPMA solid calcium content.

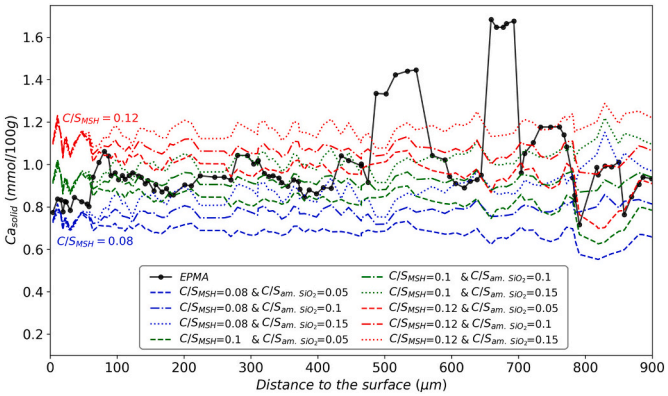

Fig. 17. Simulation of the calcium content in the solid phases for the 9 best pairs of [$C/S_{am.\ SiO2}$, C/S_{MSH}] and comparison with the EPMA solid calcium content.

The optimum intervals for C/S_{MSH} and $C/S_{am.\ SiO2}$ to match the measured Ca quantity by EPMA are in between [0.08 and 0.12] and [0.05 and 0.15], respectively. Beyond these intervals, the calcium integrated into the solid according to the calculations is much lower or higher than that measured by EPMA (Fig. 17). The curve that seems to best respect the trends of the EPMA measurements corresponds to C/S_{MSH} = 0.1 and $C/S_{am.\ SiO2}$ = 0.1. Thus, it appears that the M-S-H and amorphous silica formed contains some calcium.

The EPMA results demonstrate that the solid contains aluminium (Fig. 10). No crystallised aluminium-bearing phase was detected by XRD in the degraded zone (Fig. 12), which means that the aluminium is likely incorporated in an amorphous phase. It has been demonstrated that M-S-H, like C-S-H, can incorporate aluminium ions up to approximately A/S = 0.15–0.18 [91]. Recent work has revealed that during the degradation of cementitious phases by leaching, the siliceous gels formed can contain aluminium in significant quantities (up to A/S = 0.3 for pH = 4) [92].

Considering that aluminium can be incorporated into silica ($A/S_{am.\ SiO2}$) and M-S-H (A/S_{MSH}), the amount of calcium incorporated ($n_{Al\,solid}$) can be calculated using the following Eq. (7):

$$n_{Al\,solid} = \frac{A}{S_{MSH}} \times n_{MSH} + \frac{A}{S_{am.SiO_2}} \times n_{am.SiO_2} \quad (7)$$

with $\frac{A}{S_{MSH}}$ and $\frac{A}{S_{am.SiO_2}}$ the molar ratio of Al_2O_3 on SiO_2 in M-S-H and amorphous silica, respectively.

As for the incorporation of calcium into M-S-H and amorphous silica, simulations were carried out to find the optimum [$A/S_{am.\ SiO2}$, A/S_{MSH}]

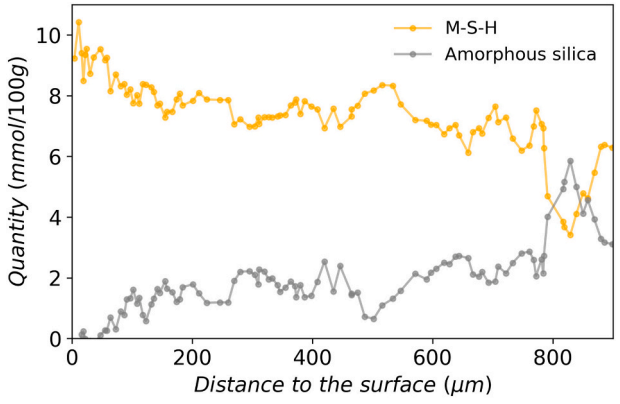

Fig. 16. Simulation of the quantities of M-S-H and amorphous silica in zone 3 of the sample exposed to $MgCl_2$ solution during 6 months.

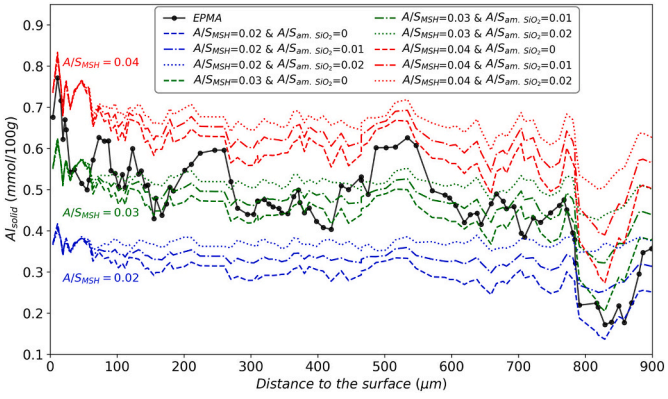

Fig. 18. Simulation of the aluminium content in the solid phases for 9 pairs of [$A/S_{am.\ SiO2}$, A/S_{MSH}] and comparison with the EPMA solid aluminium content.

pair to recover the amount of aluminium measured by EPMA, in accordance with the literature data. Fig. 18 illustrates the aluminium contents in the solid phases calculated for 9 pairs of [$A/S_{am.\ SiO2}$, A/S_{MSH}] compared to the EPMA solid aluminium content. The curve corresponding to $A/S_{MSH} = 0.03$ and $A/S_{am.\ SiO2} = 0$ seems to be the best respect to the trends of the EPMA measurements. Thus, it appears that a small amount of aluminium would be incorporated into M-S-H and would not be incorporated or very little into amorphous silica.

Fig. 19 proposes a diagram summarizing the degraded and transition zones' thicknesses and the mineralogical phases in each zone based on EDS and XRD characterizations (Figs. 9 and 12) and the previous discussion. The three degradation times are represented one below the other (2 m = 2 months, 4 m = 4 months, 6 m = 6 months). The mineralogical phases displayed in each zone are the major phases. C-S-H may be present in small quantities in the degraded zone (Z3), close to the transition zone (Z2).

In conclusion, the contact between a $MgCl_2$ solution and the model cement paste resulted in an enrichment of magnesium in the paste, corresponding to the formation of M-S-H and a silica gel – containing aluminium and calcium, associated with a decalcification of C-S-H and a sulphur leaching. After 6 months of degradation, the magnesium-enriched depth was sufficiently high (2 mm) to allow microstructural and mechanical characterization.

4.2. Evolution of microstructure

The decalcification of solid paste (Figs. 9 and 11) is known to induce porosity increase [16,93,94]. However, unlike degradation by pure water, in the case of magnesium attack, Mg bearing phases precipitate in the degraded zone (Fig. 12) and it would be expected that the increase in porosity induced by leaching would be limited.

Microtomography results show that the density in the degraded zone is half of that in the sound zone (Fig. 13). As the density is inversely proportional to the total porosity, the analyses indicate that the degraded zone is more porous than the sound zone. Thus, the formation of Mg-bearing solid phases did not fill the porosity induced by decalcification of C-S-H. The high porosity in the degraded zone may be due to the higher intrinsic porosity of the magnesium-formed phases (or lower density) than that of the C-S-H and ettringite. To discuss this hypothesis, the porosity on a smaller scale was studied by N_2 physisorption. The characterization was carried out on the degraded zone by taking and polishing pieces of samples between 0 and 1700 µm degraded for 8 months, corresponding to Zones 2 and 3 (Fig. 4). Fig. 20 and Table 5 present the results. Fig. 20 illustrates the N_2 adsorption-desorption isotherms of the sound zone and degraded zone of the degraded paste (8 months) and of a pure M-S-H paste (M/S = 0.78) [59]. Table 5 displays the Average Specific Surface B.E.T (m^2/g) calculated from the isotherms.

The degraded zone (Z2-Z3 EDS – blue curve) had a much higher specific surface area (Table 5) and a higher adsorbed amount (Fig. 20) than the sound zone (red curve), indicating a higher porosity and

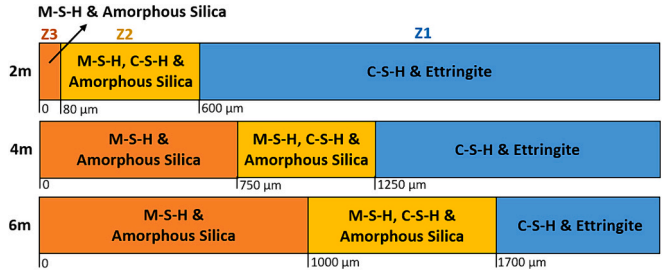

Fig. 19. Schematic representation of the chemistry of the degraded samples based on XRD, EDS and EPMA analyses, after discussion of the results. M-S-H and amorphous silica contain small amount of calcium ($C/S_{MSH} = 0.1$ and $C/S_{am.\ SiO_2} = 0.1$) and aluminium ($A/S_{MSH} = 0.03$ and $A/S_{am.\ SiO2} = 0$).

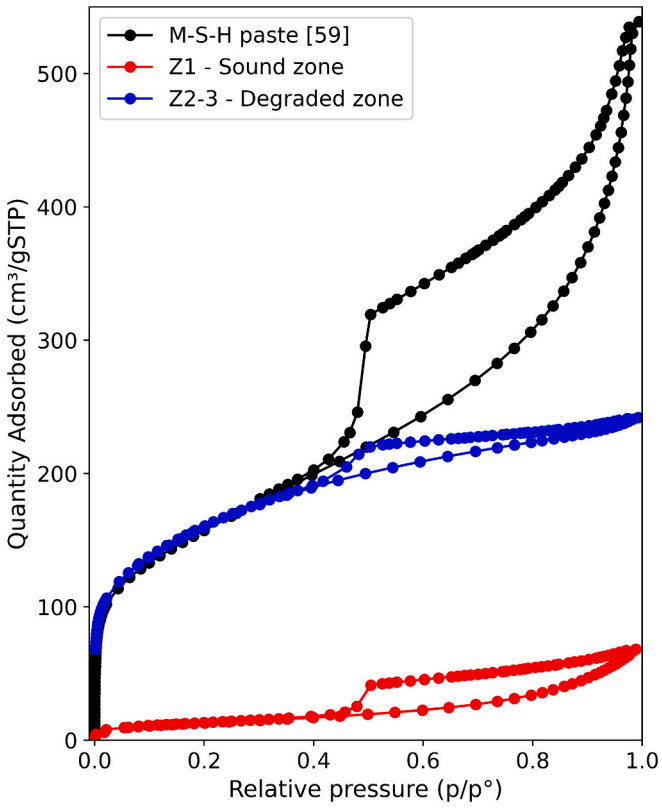

Fig. 20. N_2 adsorption-desorption isotherms of the sound zone and degraded zone, compared to a pure M-S-H paste (M/S = 0.78) [59]. Z1 = Zone 1 (sound zone) of the degraded paste (8 m), Z2–3 = Assembly of zones 2 and 3 (enriched in Mg) of the degraded paste (8 m). (For interpretation of the references to colour in this figure, the reader is referred to the web version of this article.)

Table 5
Average Specific Surface B.E.T (m^2/g) determined by N_2 Physisorption of the sound zone and degraded zone of model cement paste exposed to 5 mM $MgCl_2$ during 8 months and a M-S-H paste [59].

	Sound model cement paste	Degraded model cement paste (8 m)		M-S-H paste, M/S = 0.78
		Sound zone (Z1)	Surface (Z2-Z3)	
Average Specific Surface B.E.T (m^2/g)	36.2	53.2	571.1	562.9

confirming the observations made in micro-tomography. For comparison, the black curve with N_2 Physisorption characterization of a M-S-H paste with M/S = 0.78, developed by Dewitte et al. [59] has been added to the graph. At the small scale ($p/p_0 < 0.4$), the degraded zone had similar properties to the M-S-H pastes (i.e., the same specific surface and similar isotherm curve at the beginning). For higher p/p_0 ($p/p_0 > 0.4$), the M-S-H paste showed a larger porosity (a divergence of the sorption/desorption isotherm) than the surface of the degraded model cement paste (Z2-Z3). This could be related to the higher w/b of the M-S-H paste (1.1 vs 0.65) and/or the presence of other phases resulting from the degradation in the degraded zone (for example, amorphous silica).

In conclusion, the degraded zone - enriched in Mg, was constituted of M-S-H, showing an increased porosity compared to the sound zone, despite the formation of M-S-H. The microstructural properties observed in the Mg-enriched zone at low scale (p/p_0), showed similarities with those of synthetic M-S-H pastes and correspond to a highly porous phase. Thus, the decrease in density observed in micro-tomography could be

due to the dissolution of C-S-H and ettringite and/or to the formation of more porous phases, as M-S-H appears to be.

4.3. Elastic properties

The decrease in elastic properties (Fig. 14(c)) was progressive before reaching a plateau towards the surface and follows the trend of Ca and Mg profiles in the paste observed by EPMA (Fig. 11) and EDS (Fig. 9) at the same degradation time. According to XRD analyses (Fig. 12), the degraded zone consists mainly of M-S-H, whose Poisson's ratio is not known. To compare the observed loss of mechanical properties with those observed in the literature in the case of other chemical attacks, it is necessary to calculate a theoretical Young's modulus. Usually, the Poisson's ratio considered for a sound cementitious material is 0.24 [75,95] and that of amorphous silica is 0.19 [96]. Considering that the Poisson's ratio of the degraded zone is in this range [0.19, 0.24], the average Young's modulus of the degraded zone is estimated between 1.89 and 1.93 GPa using Eq. (8).

$$E_{deg} = \left(1-\nu^2\right) \times E_{PSIM\ (0<x<1000\ \mu m)} \text{ with } \nu_{deg} \in [0.19, 0.24] \quad (8)$$

where:

- E_{deg} is the average modulus of elasticity of the material in Zone 3
- ν_{deg} is the Poisson's ratio of the tested material in Zone 3

The uncertainty in the Poisson's ratio in the degraded zone does not therefore have a large impact on the value of the Young's modulus. Similarly, the modulus of elasticity in the sound zone can be determined according to the Eq. (9) and is equal to 10.4 GPa ($\nu = 0.24$). Thus, E_{deg}/E_{sound} (Young modulus of the degraded zone/Young modulus of the sound zone) is equal to 17.5 %.

$$E_{sound} = \left(1-0.24^2\right) \times E_{PSIM\ (2500<x<5500\ \mu m)} \quad (9)$$

where:

- E_{sound} is the average modulus of elasticity of the material in the sound zone (Z1)

Comparing this loss of elastic properties with the evolution of elastic properties in other types of chemical attacks on cement pastes helps gauge the extent of the attack. In the case of carbonation tests of a Portland cement paste (w/b = 0.5) [25,97,98], it was observed that the elastic properties at the local scale are increased at the surface (E_{deg}/E_{sound} = 220 %) compared to the sound zone. Closer to the sound zone, the properties decrease (E_{deg}/E_{sound} = 45 %) before increasing again towards the value of the sound material [97,98]. Contrary to magnesium attack, the formation of carbonate phases locally increases the elastic properties [25]. The development of cracks seems to be the primary cause of the deterioration of the elastic properties of the cement paste at a larger scale [98]. In the case of sulphate attack [29,99], the phase composition changes, soft materials and the void volume increase and the average modulus of elasticity at the local scale decreases significantly (minimal E_{deg}/E_{sound} of 12 % [29]). In the case of an ammonium nitrate solution attack to accelerate leaching, several authors have also observed a loss of elastic modulus (E_{deg}/E_{sound} between 10 % and 40 %). The residual elastic properties (E_{deg}/E_{sound}) depend on the type of phase analysed and the w/b of the cement paste. By inverse analysis on macro tests at several degradation ages, Bes [18] showed that for a material with a low C/S, E_{deg}/E_{sound} was equal to about 10 % after leaching. Brown et al. observed by nanoindentation that the most decalcified zone of a Portland cement paste, with w/b = 0.28, had an average elastic modulus of 10.9 GPa compared with 30.9 in the sound material (E_{deg}/E_{sound} = 35 %). Constantinides and Ulm carried out nanoindentation measurements on a decalcified Portland cement paste (w/b = 0.5) to observe the variations in mechanical properties associated with C-S-Hs. According to their conclusions, the volume of low-density (LD) and high-density (HD) C-S-H remain identical during decalcification, only their intrinsic properties decrease. For LD C-S-H, E_{deg}/E_{sound} is 14 % and for HD C-S-H, E_{deg}/E_{sound} is 41 %.

Thus, the loss of modulus observed in the case of magnesium attack of the presented model paste is slightly lower than that of pure leaching and sulphate attack (E_{deg}/E_{sound} of 17.5 % against 10 % to 14 %) on similar cement pastes (low C/S cement paste, LD C-S-H phase and/or w/b $\geq$ 0.5) but remains high. The formation of M-S-H does not seem to provide real compensation for the loss of mechanical properties due to the leaching and dissolution of C-S-H.

5. Conclusion

This study aimed to understand the reaction mechanisms of magnesium attack and M-S-H formation in low-calcium cementitious matrices, as well as to investigate the impact of M-S-H formation on the microstructural and mechanical properties of cementitious matrices. Chemo-mechanical and microstructural characterizations were performed on low-calcium model cement pastes exposed to 5 mM $MgCl_2$ solution for 2, 4 and 6 months.

XRD, EDS and EPMA analyses showed a homogeneous and large magnesium-enriched zone associated with the formation of M-S-H and amorphous silica. In parallel, a strong calcium and sulphur leaching, associated with C-S-H and ettringite dissolution, was observed, although calcium remained present in low proportion (Ca_{total}/Si_{total} = 0.1) without any Ca-bearing crystallised phase being detected in XRD. After stoichiometric calculations based on EPMA data, the most likely explanation is the incorporation of some calcium in the M-S-H and amorphous silica (C/S_{MSH} between 0.08 and 0.12 and $C/S_{am.\ SiO_2}$ between 0.05 and 0.15). Aluminium was also present without any Al-bearing crystallised phase being detected in XRD. According to the stoichiometric calculations, Aluminium could be integrated into M-S-H and amorphous silica to the extent of A/S_{MSH} in [0.02, 0.04] and $A/S_{am.\ SiO2}$ in [0, 0.02].

The Mg-enriched zone showed lower density (micro-tomography) and thus higher porosity than that in the sound zone. In the altered zoned where Mg content increased and Ca content decreased, the density decreased according to a comparable sigmoid. The Mg-enriched zone had similar microstructural properties to those determined on pure M-S-H pastes (N_2 Physisorption) by Dewitte et al. [59] and showed a low residual Young's modulus (15–20 % of sound zone's modulus). This drop in elastic property in the Mg enriched zone (Z3) is slightly lower but of the same order of magnitude as in pure leaching, despite the formation of M-S-H.

Funding

This work was supported by IRSN (Institut de Radioprotection et de Sûreté Nucléaire/Institute for Radiation Protection and Nuclear Safety) and INSA Toulouse (Université de Toulouse). The financial support from the European Joint Programme on Radioactive Waste (EURAD), WP MAGIC, is acknowledged.

CRediT authorship contribution statement

Charlotte Dewitte: Writing – original draft, Visualization, Validation, Methodology, Investigation, Conceptualization. **Laurie Lacarrière:** Writing – review & editing, Validation, Supervision, Resources, Project administration, Methodology, Funding acquisition, Conceptualization. **Mejdi Neji:** Writing – review & editing, Validation, Supervision, Resources, Methodology, Conceptualization. **Alexandre Dauzères:** Writing – review & editing, Validation, Supervision, Resources, Methodology, Conceptualization.

Declaration of competing interest

The authors declare that they have no known competing financial interests or personal relationships that could have appeared to influence the work reported in this paper.

Data availability

Data will be made available on request.

Appendix A. Supplementary data

Supplementary data to this article can be found online at https://doi.org/10.1016/j.cemconres.2024.107598.

References

[1] S. Carlsten, A. Strahle, C.-H. Wahlgren, P. Hultgren, L. Stenberg, H. Mattsson, Äspö Site Descriptive Model - Geological Single-Hole Interpretation of KAS04, KAS06 and KAS08, SKB, 2017.

[2] J. Smellie, C. AB, Wyoming Bentonites - Evidence From the Geological Record to Evaluate the Suitability of Bentonite as a Buffer Material During the Long-Term Underground Containment of Radioactive Wastes, SKB, 2001.

[3] Nagra, Project Opalinus Clay - Safety Report. Demonstration of Disposal Feasibility for Spent Fuel, Vitrified High-Level Waste and Long-Lived Intermediate-Level Waste (Entsorgungsnachweis), Nagra, Wettingen, Switzerland, 2002.

[4] SCK_CEN, Preparatory Safety Assessment. Conceptual Model Description of the Reference Case, SCK_CEN, Belgium, 2012.

[5] H.-J. Choi, J.Y. Lee, J. Choi, Development of geological disposal systems for spent fuels and high-level radioactive wastes in Korea, Nucl. Eng. Technol. 45 (2013) 29–40, https://doi.org/10.5516/NET.06.2012.006.

[6] H. Yoshida, K. Aoki, T. Semba, K. Ota, K. Amano, K. Hama, M. Kawamura, K. Tsubota, Overview of the stability and barrier functions of the granitic geosphere at the Kamaishi Mine: relevance to radioactive waste disposal in Japan, in: Y. Kanaori, K. Tanaka, M. Chigira (Eds.), Developments in Geotechnical Engineering, Elsevier, 2000, pp. 159–170, https://doi.org/10.1016/S0165-1250(00)80014-0.

[7] G. Escadeillas, H. Hornain, Chap 12: La durabilité des bétons vis-a-vis des environnements chimiquement agressifs, in: J.P. Ollivier, A. Vichot (Eds.), La Durabilité Des Bétons, 2008.

[8] N.M. Coleman, U. Kaktins, S. Wojno, Dam-Breach hydrology of the Johnstown flood of 1889–challenging the findings of the 1891 investigation report, Heliyon 2 (2016) e00120, https://doi.org/10.1016/j.heliyon.2016.e00120.

[9] K.R. Saxena, V.M. Sharma, Dams: Incidents and Accidents, CRC Press, 2004.

[10] NEA, Chernobyl: Assessment of Radiological and Health Impacts (2002), OECD Publishing, Paris, 2022. https://www.oecd-nea.org/jcms/pl_13598/chernobyl-assessment-of-radiological-and-health-impacts-2002?details=true. (Accessed 18 October 2023).

[13] S. Kamali, M. Moranville, S. Leclercq, Material and environmental parameter effects on the leaching of cement pastes: experiments and modelling, Cem. Concr. Res. 38 (2008) 575–585, https://doi.org/10.1016/j.cemconres.2007.10.009.

[14] J. Jain, N. Neithalath, Analysis of calcium leaching behavior of plain and modified cement pastes in pure water, Cem. Concr. Compos. 31 (2009) 176–185, https://doi.org/10.1016/j.cemconcomp.2009.01.003.

[15] C. Carde, R. François, J.-M. Torrenti, Leaching of both calcium hydroxide and C-S-H from cement paste: modeling the mechanical behavior, Cem. Concr. Res. 26 (1996) 1257–1268, https://doi.org/10.1016/0008-8846(96)00095-6.

[16] K. Wan, Q. Xu, L. Li, W. Sun, 3D porosity distribution of partly calcium leached cement paste, Construct. Build Mater. 48 (2013) 11–15, https://doi.org/10.1016/j.conbuildmat.2013.06.073.

[17] V.H. Nguyen, H. Colina, J.M. Torrenti, C. Boulay, B. Nedjar, Chemo-mechanical coupling behaviour of leached concrete: part I: experimental results, Nucl. Eng. Des. 237 (2007) 2083–2089, https://doi.org/10.1016/j.nucengdes.2007.02.013.

[18] T. Bes, Etude du comportement des bétons bas-PH sous sollicitations chimiques, These de doctorat, Toulouse 3. https://www.theses.fr/2019TOU30337, 2019 (accessed August 12, 2022).

[19] L.J. Parrott, Damage caused by carbonation of reinforced concrete, Mater. Struct. 23 (1990) 230–234, https://doi.org/10.1007/BF02473023.

[20] A. Dauzères, P. Le Bescop, C. Cau-Dit-Coumes, F. Brunet, X. Bourbon, J. Timonen, M. Voutilainen, L. Chomat, P. Sardini, On the physico-chemical evolution of low-pH and CEM I cement pastes interacting with Callovo-Oxfordian pore water under its in situ CO2 partial pressure, Cem. Concr. Res. 58 (2014) 76–88, https://doi.org/10.1016/j.cemconres.2014.01.010.

[21] L. Black, C. Breen, J. Yarwood, K. Garbev, P. Stemmermann, B. Gasharova, Structural features of C–S–H(I) and its carbonation in air—a Raman spectroscopic study. Part II: carbonated phases, Journal of the American Ceramic Society 90 (2007) 908–917, https://doi.org/10.1111/j.1551-2916.2006.01429.x.

[22] M. Auroy, S. Poyet, P. Le Bescop, J.-M. Torrenti, T. Charpentier, M. Moskura, X. Bourbon, Comparison between natural and accelerated carbonation (3% CO2): impact on mineralogy, microstructure, water retention and cracking, Cem. Concr. Res. 109 (2018) 64–80, https://doi.org/10.1016/j.cemconres.2018.04.012.

[23] Z. Šauman, Carbonization of porous concrete and its main binding components, Cem. Concr. Res. 1 (1971) 645–662, https://doi.org/10.1016/0008-8846(71)90019-6.

[24] E. Kangni-Foli, S. Poyet, P. Le Bescop, T. Charpentier, F. Bernachy-Barbé, A. Dauzères, E. L'Hôpital, J.-B. d'Espinose de Lacaillerie, Carbonation of model cement pastes: the mineralogical origin of microstructural changes and shrinkage, Cem. Concr. Res. 144 (2021) 106446, https://doi.org/10.1016/j.cemconres.2021.106446.

[25] J. Han, Y. Liang, W. Sun, W. Liu, S. Wang, Microstructure modification of carbonated cement paste with six kinds of modern microscopic instruments, J. Mater. Civ. Eng. 27 (2015) 04014262, https://doi.org/10.1061/(ASCE)MT.1943-5533.0001210.

[26] M. Santhanam, M.D. Cohen, J. Olek, Sulfate attack research — whither now? Cem. Concr. Res. 31 (2001) 845–851, https://doi.org/10.1016/S0008-8846(01)00510-5.

[27] M. Santhanam, M.D. Cohen, J. Olek, Mechanism of sulfate attack: a fresh look: part 1: summary of experimental results, Cem. Concr. Res. 32 (2002) 915–921, https://doi.org/10.1016/S0008-8846(02)00724-X.

[28] M. Santhanam, M.D. Cohen, J. Olek, Mechanism of sulfate attack: a fresh look: part 2. Proposed mechanisms, Cement and Concrete Research 33 (2003) 341–346, https://doi.org/10.1016/S0008-8846(02)00958-4.

[29] J. Pouya, M. Neji, L. De Windt, F. Péralès, A. Socié, J. Corvisier, Mineralogical evolution and expansion of cement pastes in a sulfate-confined environment, Minerals 13 (2023) 1, https://doi.org/10.3390/min13010001.

[30] D. Hou, T. Li, P. Wang, Molecular dynamics study on the structure and dynamics of NaCl solution transport in the nanometer channel of CASH gel, ACS Sustain. Chem. Eng. 6 (2018) 9498–9509, https://doi.org/10.1021/acssuschemeng.8b02126.

[31] B. Martín-Pérez, H. Zibara, R.D. Hooton, M.D.A. Thomas, A study of the effect of chloride binding on service life predictions, Cem. Concr. Res. 30 (2000) 1215–1223, https://doi.org/10.1016/S0008-8846(00)00339-2.

[32] O. Francy, Modelisation de la penetration des ions chlorures dans les mortiers partiellement satures en eau, These de doctorat, Toulouse 3. https://www.theses.fr/1998TOU30219, 1998 (accessed October 13, 2022).

[33] G.K. Glass, N.R. Buenfeld, Chloride-induced corrosion of steel in concrete, Prog. Struct. Eng. Mater. 2 (2000) 448–458, https://doi.org/10.1002/pse.54.

[34] J. Yang, D. Hou, Q. Ding, G. Zhang, Y. Zhang, H. Hu, Insight on the nanoscale chemical degradation mechanism of MgCl2 attack in cement paste, Construct. Build Mater. 238 (2020) 117777, https://doi.org/10.1016/j.conbuildmat.2019.117777.

[35] N. Xie, Y. Dang, X. Shi, New insights into how MgCl2 deteriorates Portland cement concrete, Cem. Concr. Res. 120 (2019) 244–255, https://doi.org/10.1016/j.cemconres.2019.03.026.

[36] C. Qiao, P. Suraneni, M. Tsui Chang, J. Weiss, Damage in cement pastes exposed to MgCl2 solutions, Mater Struct 51 (2018) 74, https://doi.org/10.1617/s11527-018-1191-2.

[37] A. Neville, Chloride attack of reinforced concrete: an overview, Materials and Structures 28 (1995) 63–70, https://doi.org/10.1007/BF02473172.

[38] M. Pigeon, Durability of Concrete in Cold Climates, CRC Press, 2014.

[39] M. Rosenqvist, A. Bertron, K. Fridh, M. Hassanzadeh, Concrete alteration due to 55years of exposure to river water: chemical and mineralogical characterisation, Cem. Concr. Res. 92 (2017) 110–120, https://doi.org/10.1016/j.cemconres.2016.11.012.

[40] U.H. Jakobsen, Microstructural surface deterioration of concrete exposed to seawater; results after 2 years exposure, in: 14th Euroseminar on Microscopy Applied to Building Materials, 2013, pp. 10–14.

[41] C. Lerouge, S. Gaboreau, S. Grangeon, F. Claret, F. Warmont, A. Jenni, V. Cloet, U. Mäder, In situ interactions between Opalinus Clay and Low Alkali Concrete, Physics and Chemistry of the Earth, Parts A/B/C 99 (2017) 3–21, https://doi.org/10.1016/j.pce.2017.01.005.

[42] J.L. García Calvo, A. Hidalgo, C. Alonso, L. Fernández Luco, Development of low-pH cementitious materials for HLRW repositories: resistance against ground waters aggression, Cem. Concr. Res. 40 (2010) 1290–1297, https://doi.org/10.1016/j.cemconres.2009.11.008.

[43] K. De Weerdt, H. Justnes, The effect of sea water on the phase assemblage of hydrated cement paste, Cement and Concrete Composites 55 (2015) 215–222, https://doi.org/10.1016/j.cemconcomp.2014.09.006.

[44] U.H. Jakobsen, K. De Weerdt, M.R. Geiker, Elemental zonation in marine concrete, Cem. Concr. Res. 85 (2016) 12–27, https://doi.org/10.1016/j.cemconres.2016.02.006.

[45] A. Dauzeres, G. Achiedo, D. Nied, E. Bernard, S. Alahrache, B. Lothenbach, Magnesium perturbation in low-pH concretes placed in clayey environment—solid characterizations and modeling, Cem. Concr. Res. 79 (2016) 137–150, https://doi.org/10.1016/j.cemconres.2015.09.002.

[46] E. Bernard, B. Lothenbach, F. Le Goff, I. Pochard, A. Dauzères, Effect of magnesium on calcium silicate hydrate (C-S-H), Cem. Concr. Res. 97 (2017) 61–72, https://doi.org/10.1016/j.cemconres.2017.03.012.

[47] E. Bernard, B. Lothenbach, C. Cau-Dit-Coumes, C. Chlique, A. Dauzères, I. Pochard, Magnesium and calcium silicate hydrates, part I: investigation of the possible magnesium incorporation in calcium silicate hydrate (C-S-H) and of the calcium in magnesium silicate hydrate (M-S-H), Appl. Geochem. 89 (2018) 229–242, https://doi.org/10.1016/j.apgeochem.2017.12.005.

[48] B. Lothenbach, F. Winnefeld, Thermodynamic modelling of the hydration of Portland cement, Cem. Concr. Res. 36 (2006) 209–226, https://doi.org/10.1016/j.cemconres.2005.03.001.

[49] A. Vollpracht, B. Lothenbach, R. Snellings, J. Haufe, The pore solution of blended cements: a review, Mater Struct 49 (2016) 3341–3367, https://doi.org/10.1617/s11527-015-0724-1.
[50] C.L. Page, Ø. Vennesland, Pore solution composition and chloride binding capacity of silica-fume cement pastes, Mater. Constr. 16 (1983) 19–25, https://doi.org/10.1007/BF02474863.
[51] M.H. Shehata, M.D.A. Thomas, R.F. Bleszynski, The effects of fly ash composition on the chemistry of pore solution in hydrated cement pastes, Cem. Concr. Res. 29 (1999) 1915–1920, https://doi.org/10.1016/S0008-8846(99)00190-8.
[52] X. Liu, P. Feng, X. Yu, X. Shen, G. Geng, B. Lothenbach, The physiochemical alterations of calcium silicate hydrate (C-S-H) under magnesium attack, Cem. Concr. Res. 160 (2022) 106901, https://doi.org/10.1016/j.cemconres.2022.106901.
[53] D. Nied, K. Enemark-Rasmussen, E. L'Hopital, J. Skibsted, B. Lothenbach, Properties of magnesium silicate hydrates (M-S-H), Cem. Concr. Res. 79 (2016) 323–332, https://doi.org/10.1016/j.cemconres.2015.10.003.
[54] E. Bernard, B. Lothenbach, C. Chlique, M. Wyrzykowski, A. Dauzères, I. Pochard, C. Cau-Dit-Coumes, Characterization of magnesium silicate hydrate (M-S-H), Cem. Concr. Res. 116 (2019) 309–330, https://doi.org/10.1016/j.cemconres.2018.09.007.
[55] C. Roosz, P. Vieillard, P. Blanc, S. Gaboreau, H. Gailhanou, D. Braithwaite, V. Montouillout, R. Denoyel, P. Henocq, B. Madé, Thermodynamic properties of C-S-H, C-A-S-H and M-S-H phases: results from direct measurements and predictive modelling, Appl. Geochem. 92 (2018) 140–156, https://doi.org/10.1016/j.apgeochem.2018.03.004.
[56] C. Roosz, S. Grangeon, P. Blanc, V. Montouillout, B. Lothenbach, P. Henocq, E. Giffaut, P. Vieillard, S. Gaboreau, Crystal structure of magnesium silicate hydrates (M-S-H): the relation with 2: 1 Mg–Si phyllosilicates, Cem. Concr. Res. 73 (2015) 228–237, https://doi.org/10.1016/j.cemconres.2015.03.014.
[57] D.R.M. Brew, F.P. Glasser, Synthesis and characterisation of magnesium silicate hydrate gels, Cem. Concr. Res. 35 (2005) 85–98, https://doi.org/10.1016/j.cemconres.2004.06.022.
[58] B. Lothenbach, D. Nied, E. L'Hôpital, G. Achiedo, A. Dauzères, Magnesium and calcium silicate hydrates, Cem. Concr. Res. 77 (2015) 60–68, https://doi.org/10.1016/j.cemconres.2015.06.007.
[59] C. Dewitte, A. Bertron, M. Neji, L. Lacarrière, A. Dauzères, Chemical and microstructural properties of designed cohesive M-S-H pastes, Materials 15 (2022) 547, https://doi.org/10.3390/ma15020547.
[60] T. Zhang, L.J. Vandeperre, C.R. Cheeseman, Formation of magnesium silicate hydrate (M-S-H) cement pastes using sodium hexametaphosphate, Cem. Concr. Res. 65 (2014) 8–14, https://doi.org/10.1016/j.cemconres.2014.07.001.
[61] C. Sonat, C. Unluer, Development of magnesium-silicate-hydrate (M-S-H) cement with rice husk ash, J. Clean. Prod. 211 (2019) 787–803, https://doi.org/10.1016/j.jclepro.2018.11.246.
[62] S. Hesaraki, A. Zamanian, F. Moztarzadeh, Effect of adding sodium hexametaphosphate liquefier on basic properties of calcium phosphate cements, J. Biomed. Mater. Res. A 88A (2009) 314–321, https://doi.org/10.1002/jbm.a.31836.
[63] Y. Jia, B. Wang, Z. Wu, J. Han, T. Zhang, L.J. Vandeperre, C.R. Cheeseman, Role of sodium hexametaphosphate in MgO/SiO2 cement pastes, Cem. Concr. Res. 89 (2016) 63–71, https://doi.org/10.1016/j.cemconres.2016.08.003.
[64] M. Tonelli, F. Martini, A. Milanesi, L. Calucci, M. Geppi, S. Borsacchi, F. Ridi, Effect of phosphate additives on the hydration process of magnesium silicate cements, J. Therm. Anal. Calorim. 138 (2019) 3311–3321, https://doi.org/10.1007/s10973-019-08847-9.
[75] G. Constantinides, F.-J. Ulm, The effect of two types of C-S-H on the elasticity of cement-based materials: results from nanoindentation and micromechanical modeling, Cem. Concr. Res. 34 (2004) 67–80, https://doi.org/10.1016/S0008-8846(03)00230-8.
[77] L. Sutter, K. Peterson, S. Touton, T. Van Dam, D. Johnston, Petrographic evidence of calcium oxychloride formation in mortars exposed to magnesium chloride solution, Cem. Concr. Res. 36 (2006) 1533–1541, https://doi.org/10.1016/j.cemconres.2006.05.022.
[78] A. Bertron, G. Escadeillas, P. de Parseval, J. Duchesne, Processing of electron microprobe data from the analysis of altered cementitious materials, Cem. Concr. Res. 39 (2009) 929–935, https://doi.org/10.1016/j.cemconres.2009.06.011.
[79] M. Giroudon, Evaluation des interactions entre biodéchets en digestion anaérobie et matériaux cimentaires à base de différents liants en vue d'une meilleure durabilité des structures de méthanisation, These de doctorat, Toulouse, INSA. http://www.theses.fr/2021ISAT0001, 2021.
[80] E.P. Barrett, L.G. Joyner, P.P. Halenda, The determination of pore volume and area distributions in porous substances. I. Computations from nitrogen isotherms, J. Am. Chem. Soc. 73 (1951) 373–380, https://doi.org/10.1021/ja01145a126.
[81] J. Fu, S. Kamali-Bernard, F. Bernard, M. Cornen, Comparison of mechanical properties of C-S-H and portlandite between nano-indentation experiments and a modeling approach using various simulation techniques, Compos. Part B Eng. 151 (2018) 127–138, https://doi.org/10.1016/j.compositesb.2018.05.043.
[82] O. Maciejak, P. Aubert, Mesure de dureté par nano-indentation, Ref: TIP155WEB - "Nanosciences et nanotechnologies". https://www.techniques-ingenieur.fr/base-documentaire/innovation-th10/nanosciences-concepts-simulation-et-caracterisation-42194210/mesure-de-durete-par-nano-indentation-nm7200/, 2007. (Accessed 26 May 2020).
[83] D.L. Nguyen, Nouvelle méthodologie d'identification des propriétés mécaniques locales d'un matériau hétérogène par nanoindentation: application aux matériaux du génie civil, thesis, Paris Est. http://www.theses.fr/2017PESC1028, 2017.
[84] F.-J. Ulm, M. Vandamme, H.M. Jennings, J. Vanzo, M. Bentivegna, K.J. Krakowiak, G. Constantinides, C.P. Bobko, K.J. Van Vliet, Does microstructure matter for statistical nanoindentation techniques? Cement and Concrete Composites 32 (2010) 92–99, https://doi.org/10.1016/j.cemconcomp.2009.08.007.
[85] P. Trtik, B. Münch, P. Lura, A critical examination of statistical nanoindentation on model materials and hardened cement pastes based on virtual experiments, Cement and Concrete Composites 31 (2009) 705–714, https://doi.org/10.1016/j.cemconcomp.2009.07.001.
[86] Z. Hu, M. Wyrzykowski, M. Griffa, K. Scrivener, P. Lura, Young's modulus and creep of calcium-silicate-hydrate compacts measured by microindentation, Cem. Concr. Res. 134 (2020) 106104, https://doi.org/10.1016/j.cemconres.2020.106104.
[87] J.J. Chen, L. Sorelli, M. Vandamme, F.-J. Ulm, G. Chanvillard, A coupled nanoindentation/SEM-EDS study on low water/cement ratio Portland cement paste: evidence for C–S–H/Ca(OH)2 nanocomposites, J. Am. Ceram. Soc. 93 (2010) 1484–1493, https://doi.org/10.1111/j.1551-2916.2009.03599.x.
[88] AFNOR, Béton - Définition et classification des environnements chimiquement agressifs - Recommandations pour la formulation des bétons. https://www.boutique.afnor.org/fr-fr/norme/fd-p18011/beton-definition-et-classification-des-environnements-chimiquement-agressif/fa204582/328696, 2022. (Accessed 17 November 2023).
[89] AFNOR, Béton - Spécification, performances, production et conformité. https://www.boutique.afnor.org/fr-fr/norme/nf-en-206/beton-specification-performances-production-et-conformite/fa171582/1465, 2014. (Accessed 17 November 2023).
[90] E. Bernard, A. Dauzères, B. Lothenbach, Magnesium and calcium silicate hydrates, part II: Mg-exchange at the interface "low-pH" cement and magnesium environment studied in a C-S-H and M-S-H model system, Appl. Geochem. 89 (2018) 210–218, https://doi.org/10.1016/j.apgeochem.2017.12.006.
[91] E. Bernard, B. Lothenbach, C. Cau-Dit-Coumes, I. Pochard, D. Rentsch, Aluminum incorporation into magnesium silicate hydrate (M-S-H), Cem. Concr. Res. 128 (2020) 105931, https://doi.org/10.1016/j.cemconres.2019.105931.
[92] C. Roosz, M. Giroudon, L. Lacarriere, M. Peyre-Lavigne, C. Patapy, A. Bertron, New insights into aluminosilicate gel from acetic acid attack of hydrated Portland cement: experimental and thermodynamic characterization, Appl. Geochem. 162 (2023) 105923, https://doi.org/10.1016/j.apgeochem.2024.105923.
[93] C. Carde, R. François, Modelling the loss of strength and porosity increase due to the leaching of cement pastes, Cement and Concrete Composites 21 (1999) 181–188, https://doi.org/10.1016/S0958-9465(98)00046-8.
[94] S. Kamali, M. Moranville, E. Garboczi, S. Prené, B. Gérard, Hydrate Dissolution Influence on the Young's Modulus of Cement Pastes. https://framcos.org/FraMCoS-5/kamali.hydrate.pdf, 2004.
[95] P. Mondal, S.P. Shah, L. Marks, A reliable technique to determine the local mechanical properties at the nanoscale for cementitious materials, Cem. Concr. Res. 37 (2007) 1440–1444, https://doi.org/10.1016/j.cemconres.2007.07.001.
[96] M. Arnold, A.R. Boccaccini, G. Ondracek, Prediction of the Poisson's ratio of porous materials, J. Mater. Sci. 31 (1996) 1643–1646, https://doi.org/10.1007/BF00357876.
[97] Q. Li, Y.M. Lim, Y.-S. Jun, Effects of sulfate during CO2 attack on Portland cement and their impacts on mechanical properties under geologic CO2 sequestration conditions, Environ. Sci. Technol. 49 (2015) 7032–7041, https://doi.org/10.1021/es506349u.
[98] Q. Li, Y.M. Lim, K.M. Flores, K. Kranjc, Y.-S. Jun, Chemical reactions of Portland cement with aqueous CO2 and their impacts on cement's mechanical properties under geologic CO2 sequestration conditions, Environ. Sci. Technol. 49 (2015) 6335–6343, https://doi.org/10.1021/es5063488.
[99] C. Qian, Y. Nie, T. Cao, Sulphate attack-induced damage and micro-mechanical properties of concrete characterized by nano-indentation coupled with X-ray computed tomography, Struct. Concr. 17 (2016) 96–104, https://doi.org/10.1002/suco.201400123.